

## Model-based interpretation of sediment concentration and vertical flux measurements in a shallow estuarine environment

Andreas Brand,<sup>\*1,2,3</sup> Jessica R. Lacy,<sup>4</sup> Steve Gladding,<sup>1</sup> Rusty Holleman,<sup>1</sup> Mark Stacey<sup>1</sup>

<sup>1</sup>Department of Civil and Environmental Engineering, University of California, Berkeley, California

<sup>2</sup>Department of Surface Waters – Research and Management, Swiss Federal Institute of Aquatic Science and Technology (Eawag), Kastanienbaum, Switzerland

<sup>3</sup>Institute of Biogeochemistry and Pollutant Dynamics, Swiss Federal Institute of Technology (ETH), Zurich, Switzerland

<sup>4</sup>Pacific Coastal and Marine Science Center, U.S. Geological Survey, Santa Cruz, California

### Abstract

A one-dimensional numerical model describing tidally varying vertical mixing and settling was used to interpret sediment concentrations and vertical fluxes observed in the shoals of South San Francisco Bay by two acoustic Doppler velocimeters (ADV) at elevations of 0.36 m and 0.72 m above bed. Measured sediment concentrations changed by up to 100 g m<sup>-3</sup> over the semidiurnal tidal cycle. These dynamics were dominated by local resuspension and settling. Multiple particle class models suggested the existence of a class with fast settling velocities ( $w_s$  of  $9.0 \times 10^{-4}$  m s<sup>-1</sup> in spring and  $5.8 \times 10^{-4}$  m s<sup>-1</sup> in fall) and a slowly settling particle fraction ( $w_s$  of  $<1 \times 10^{-7}$  m s<sup>-1</sup> in spring and  $1.4 \times 10^{-5}$  m s<sup>-1</sup> in fall). Modeled concentrations of slowly settling particles at 0.36 m were as high as 20 g m<sup>-3</sup> during fall and varied with the spring-neap cycle while fine sediment concentrations in spring were constant around 5 g m<sup>-3</sup>. Analysis of in situ water column floc size distributions suggested that floc properties in the lower part of the water column were most likely governed by particle-size distribution on the bed and not by coagulation, validating our multiple particle size approach. A comparison of different sediment bed models with respect to model performance, sensitivity, and identifiability suggested that the use of a sediment erosion model linear in bottom shear stress  $\tau_b$  ( $E = M (\tau_b - \tau_c)$ ) was the most appropriate choice to describe the field observations when the critical shear stress  $\tau_c$  and the proportionality factor  $M$  were kept constant.

Suspended sediment is one of the driving influences for water quality in lakes, rivers, and estuaries. Compared to bed sediment, suspended sediment is more reactive due to its higher accessible surface area (Tengberg et al. 2003). Therefore, erosion events can lead to increased mineralization of suspended particles which triggers increased consumption of oxygen in the water column and elevated nutrient release from the sediment particles (Wainright and Hopkinson 1997). This elevated nutrient release can result in an increase in primary production (Ogilvie and Mitchell 1998). Conversely, suspended sediment can also inhibit algal growth by decreasing the light penetration depth (Cloern 1987). Suspended sediment is also important for the release and sorption of organic and inorganic contaminants like polychlorinated hydrocarbons and mercury (Schoellhamer et al. 2007). To assess the impact of suspended sediment dynamics in a system, it is important to characterize mixing,

flocculation, and settling of sediment particles in the water column as well as the resuspension of sediment from the bed. Still, many of the parameters controlling these processes are difficult to measure. Direct in situ determination of sediment bed properties and settling velocities require complex analytical devices, while measurements in the laboratory cannot reproduce in situ conditions and therefore may change sediment properties. As an alternative approach, sediment properties can be estimated by analyzing sediment concentrations and fluxes observed in the field using numerical models.

The one-dimensional (1D) sediment transport equation in a tidal system can be written as

$$\frac{\partial C}{\partial t} = -\frac{\partial(w-w_s)C}{\partial z} + \frac{\partial}{\partial z} \left( \varepsilon_s \frac{\partial C}{\partial z} \right) + S_h \quad (1)$$

where  $C$  is the sediment concentration,  $w$  the vertical velocity due to the change in tidal elevation and  $w_s$  the settling velocity,  $\varepsilon_s$  the vertical turbulent sediment diffusivity,  $z$  the

\*Correspondence: andreas.brand@eawag.ch

vertical coordinate.  $S_h$  is the source term due to horizontal transport processes.  $\varepsilon_s$  is related to the eddy viscosity  $\nu_T$  by the inverse turbulent Schmidt number  $\beta$  for sediment transport (e.g., Dyer and Soulsby 1988)

$$\beta = \frac{\varepsilon_s}{\nu_T}. \quad (2)$$

In shallow, vertically well mixed tidal systems,  $\nu_T$  is frequently described by the parabolic law for unstratified channel flow (e.g., Dyer and Soulsby 1988; Kineke and Sternberg 1989):

$$\nu_T = \kappa u_* z \left(1 - \frac{z}{H}\right) \quad (3)$$

where  $\kappa$  is the von Karman constant,  $u_*$  the shear velocity, and  $H$  the height of the water column.

Many studies of near-bed suspended sediment dynamics assume a negligible  $w$  and a steady state between upward diffusion and settling due to gravity ( $\partial C/\partial t = 0$ ) as well as negligible sources from horizontal sediment advection ( $S_h = 0$ ) (e.g., Sternberg et al. 1986). Eq. 1 can then be simplified to:

$$\varepsilon_s \frac{\partial C}{\partial z} = -w_s C \quad (4)$$

$w_s$  can be determined by fitting the Rouse equation, which results from Eqs. 2, 3, and 4 to observed sediment profiles (Kineke and Sternberg 1989; Drake and Cacchione 1989). Settling tubes can provide direct measurements of  $w_s$  (Pejrup and Mikkelsen 2010). The combined use of settling tubes with floc cameras (Manning and Dyer 2007) or laser scattering particles size analyzers like the LISST (Agrawal and Pottsmith 2000) can provide additional information on in situ particle size and density.

Sediment bed erosion occurs when the bottom shear stress  $\tau_b$  exceeds the critical shear stress  $\tau_{crit}$ . A commonly used empirical equation for the sediment erosion rate  $E$  is

$$E = M_z(z_E)(\tau_b - \tau_{crit}(z_E))^k, \quad (5)$$

where  $M$  and  $k$  are empirical constants (Sanford and Maa 2001). Eq. 5 has been used to represent situations when the critical shear stress increases with depth below the seafloor and limits the extent of erosion (Type I erosion) (Sanford and Maa 2001). If the sediment porosity is constant, the erosion depth  $z_E$  is directly proportional to the resuspended mass  $m_R$ . Following Sanford and Maa (2001), we assume a linear increase in  $\tau_{crit}$  and  $M_z$  with  $m_R$  and a  $k$  value of 1:

$$E = (M_0 + \mu m_R)(\tau_b - (\tau_{crit,0} + \beta m_R)), \quad (6)$$

where  $\mu$  and  $\beta$  are the proportionality constants and  $M_0$  and  $\tau_{crit,0}$  are the values at the uneroded sediment surface. In many cases, simplified versions of Eq. 5 are used like the linear erosion model

$$E = M(\tau_b - \tau_{crit}), \quad (7)$$

which is based on a constant critical shear stress throughout the sediment profile (Type II erosion) (Sanford and Maa 2001). Another approach assumes a nonlinear relationship while not considering  $\tau_{crit}$  explicitly (Sanford and Halka 1993, Zimmerman et al. 2008)

$$E = M(\tau_b)^k \quad (8)$$

We will refer to Eq. 8 as the nonlinear erosion model.  $M$ ,  $k$ , and  $\tau_{crit}$  vary widely between field sites as they depend on sediment material properties such as particle grain size and organic carbon content as well as on the salinity of the pore water. In addition, the bed erosion models described by Eqs. 5, 6, 7, and 8 do not account for the fact that  $\tau_{crit}$  depends on the transient history of the sediment bed erosion, deposition and consolidation. More sophisticated models have become available recently, which consider these short term effects (e.g., Sanford 2008).

In the presented article, we determine sediment erosion as a linear function of the turbulent sediment flux  $\overline{w'C'}$  observed in the water column as a first estimate.

$$E = \text{amp} \times \overline{w'C'} \quad (9)$$

where amp is the entrainment amplification factor. In the remainder of the manuscript we will call this approach the flux amplification method. We chose this approach because the turbulent sediment flux responds directly to processes like loosening, consolidation and erosion limitation by depth-dependent critical shear stress and bed armoring. As we will show in this manuscript, we can use the erosion model based on Eq. 9 to estimate the parameters of more predictive bed erosion models like those based on Eq. 7 or 8. This approach allows us to investigate sediment properties in situ under minimal disturbance caused by the equipment. While laboratory experiments allow detailed studies of sediment under controlled conditions, their results may not be sufficiently representative of the conditions in the field (Tolhurst et al. 2009; Kleeberg et al. 2008), as sampling, storage, and transport alter the properties of the cohesive, thixotropic sediment. Numerous instruments have been developed to characterize sediment resuspension in the field, but these instruments are generally difficult to build and not commercially available. In addition, such in situ benthic flumes do not necessarily reflect the properties of the undisturbed sediment. For example, it was found that the erosion threshold is reduced when sediments are exposed to standing water prior to an experimental run (Tolhurst et al. 2009).

As it is commonly used in model studies of sediment transport in natural systems (Amoudry and Souza 2011), we assume that simultaneous erosion and continuous deposition occurs such that the net influx into the water column is the difference between erosion  $E$  and the deposition  $D$

$$D = w_s C|_{z=0} \quad (10)$$

Our model also allows resuspension of various particle classes from the sediment. We assumed that the bed erosion of each particle size class  $i$  is proportional to the total sediment erosion:

$$E_i = \alpha_i E, \quad (11)$$

where  $\alpha_i$  is the fraction of particle class  $i$  in the eroded bed sediment. Many models include also a critical deposition stress above which no sediment deposition occurs (e.g., Ha and Maa 2009). Still such a deposition stress was mainly observed in laboratory experiments and its existence under field conditions is still questioned (Winterwerp and van Kesteren 2004). Therefore we decided to include the model without deposition stress.

Brand et al. (2010) presented an analysis of sediment concentration, turbulent sediment flux and bottom shear data obtained from acoustic Doppler velocimeter (ADV) velocity and acoustic backscatter data from a field campaign in a shallow, wind wave affected field site in South San Francisco Bay in spring 2009. They observed a strong increase in turbulent sediment flux under the simultaneous presence of wind waves and turbulence. The comparison between disaggregated grain size analyses and particle-size distributions obtained in situ using laser scattering showed that the resuspended particles consist of aggregated flocs. Brand et al. (2010) focused their analysis on the measured turbulent sediment flux and its relation to current and wave induced bottom shear which was calculated with the Styles and Glenn (2000) model. In this manuscript we present an additional data set obtained in fall 2009 at the same field site and extend the analysis of the data by inferring sediment bed and resuspended particle properties using a 1D sediment transport and mixing model. Due to the shallowness of the field site, tidal dynamics changed the water column depth by more than 50%. As the height of the water column defined the volume in which the eroded sediment is distributed, we expected a strong dependence of the sediment concentration on tidal elevation. In addition we used model performance measures, sensitivity and identifiability analysis to assess different sediment bed erosion models.

## Field Setup and Data Evaluation

### Field campaign

The study was conducted in South San Francisco Bay at a shallow water site south of San Mateo Bridge on the eastern edge of the deep channel which bisects the Bay. The South Bay generally refers to the part of the San Francisco Bay south of the Bay Bridge connecting San Francisco and Oakland (Fig. 1). It is characterized by two broad shoals (each 2–4 m deep) which are divided by a deep channel (approximately 14 m mean lower low water, (MLLW)). The

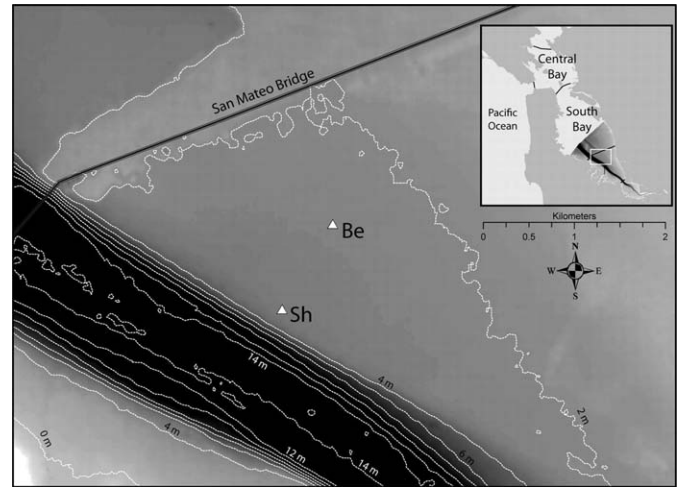


**Fig. 1.** Location of study site and field stations. Be: main station closer to the shore at 2.19 m MLLW elevation. Sh: additional station at 2.59 m MLLW elevation closer to the channel (taken from Brand et al. 2010).

hydrodynamics of this part of the bay are controlled by tides, winds, and freshwater runoff.

An instrument platform (Be station in Fig. 1) was deployed as part of a larger-scale study in the shallow waters of the San Francisco South Bay (Lon: 122.20977, Lat: 37.58633, depth 2.19 m MLLW) during two campaigns from 02/24/2009 to 03/16/2009 and from 09/09/2009 to 10/07/2009. We will refer to these campaigns as the spring and the fall campaign respectively. The instrument platform was equipped with two 10 MHz ADVs (Sontek Hydra) which recorded 8 minute bursts at 10 Hz every 12 min at 0.36 and 0.72 m above the bottom. The particle-size distributions of suspended sediment were determined in situ using a LISST 100 Type B (size range 1.2–250  $\mu\text{m}$ , Sequoia Scientific Inc.) mounted 0.55 m above the bed. An additional Sontek 10 MHz ADV was deployed 1000 m closer to the channel than our primary field site (Lat:37.5830, Lon: 122.2205, elevation 2.59 m MLLW) at 0.45 m elevation above the bed (Sh station in Fig. 1).

Sediment samples were taken using a Ponar sediment sampler. The sediments consisted of a muddy, fluffy top layer of sediment which covers a layer of strongly consolidated mud. The fluffy top layer was carefully scraped off for particle size analysis. The sediment samples were disaggregated before grain size analysis using ultrasonification after treatment with hydrogen peroxide and carbonates were removed using calgon. The grain size distribution was measured using a Beckman Coulter Laser Sizer particle analyzer.

The ADVs were calibrated against sediment concentrations determined from water samples taken during the field campaign. Approximately one liter of water was pumped from a submersible sampling unit which was deployed close (<30 m distance) to each measurement station. The unit

consisted of a vertical pole mounted on a platform. Tubing was fixed on the vertical pole at the same elevations as the ADVs. The water samples were pumped to the surface using a peristaltic pump. The samples were filtered through pre-weighted 0.4  $\mu\text{m}$  filters (Whatman Nucleopore). The filtration units were flushed three times with freshwater to remove the salt of the brackish bay water. The filters were dried at 60°C for 24 h and the sediment mass was determined as the difference of filter weight before and after filtration. For details of this procedure and typical calibrations see Brand et al. (2010).

Turbulent sediment fluxes and shear velocities were determined from the ADV data. To remove wave contamination from the turbulent quantities, we used the method of Shaw and Trowbridge (2001). In addition, we performed a coordinate system rotation following Lee et al. (2004) to remove any contamination of the vertical velocity by horizontal velocity components before calculation of the Reynolds shear stress.

### Water column model

The water column model was based on a first-order finite volume formulation of Eq. 1:

$$\frac{\partial hC}{\partial t} = q_{up} - q_{low} + \int_h S_h dz = \left( \varepsilon_{s,up} \frac{\partial C}{\partial z} \Big|_{up} - w_s C \Big|_{up} \right) - \left( \varepsilon_{s,low} \frac{\partial C}{\partial z} \Big|_{low} - w_s C \Big|_{low} \right) + \int_h S_h dz \quad (12)$$

where  $h$  is the thickness of the grid cell and  $q_{up}$  and  $q_{low}$  the fluxes at the upper and the lower boundary of the cell (Fig. 2). The indices up and low denote the upper and lower boundary of the grid cell. The sediment concentrations and gradients at the cell interfaces were determined using linear interpolation. Our model accounted for the change in water depth  $H$  by tides by adjusting the thickness of the grid cell  $h$ . The temporal development over a day during the spring campaign of a grid based on 20 grid cells is shown in Fig. 2. The actual model runs in this study were performed using 60 grid cells. The details of this calculation and the grid adaption algorithm can be found in Appendix A. The change in tidal elevation results in an horizontal inflow of water and sediment

$$S_h = \frac{\partial(uC)}{\partial x} = u \frac{\partial C}{\partial x} + C \frac{\partial u}{\partial x} \quad (13)$$

where  $u$  is the horizontal velocity and  $x$  the along stream coordinate. Assuming that the sediment concentration was locally horizontally homogenous - we will show later that this assumption is valid-, the first term at the right-hand side of Eq. 13 becomes negligible and the change in sediment mass and water volume is mainly due to the advection of water with a horizontally constant sediment concentration. To account for the change in water mass due to tides, we changed the size of each grid cell  $j$  at each time step by

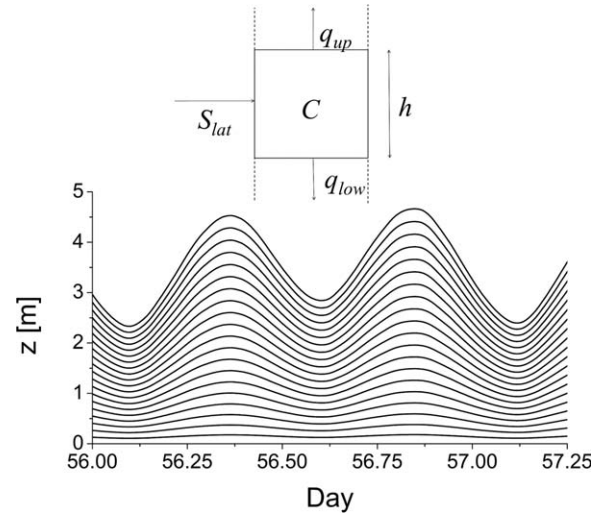


**Fig. 2.** Sketch of a grid cell as described by Eq. 12.  $h$ : height of the grid cell,  $C$ : sediment concentration at the center of the cell,  $q_{up}$ : flux at the upper cell boundary,  $q_{low}$ : flux at the lower cell boundary,  $S_h$ : source term due to horizontal inflow and outflow and temporal development of a water column discretization using 20 grid cells over a day during the spring campaign.

$\Delta h_j$ .  $\Delta h_j$  is calculated based on the vertical velocity profile and the horizontal velocity gradient (see Appendix A). The adaptation to the tidal elevation results in a change in mass in the  $j$ th grid cell by  $\Delta M_j = \int_{\Delta t} \int_h S_{h,j} dz dt = C_j \Delta h_j$ .

The calculation of the turbulent diffusion coefficients using Eqs. 2 and 3 requires  $u_*$ . Since a part of the Reynolds stress measurements by the ADVs during the spring campaign were disturbed by the frames of the monitoring stations, it was necessary to estimate  $u_*$  values to close the data gaps using following approach: first, we estimate  $z_0$  values from Reynolds stresses measured at 0.36 m ( $u_* = \sqrt{u'w'}$ , where  $u'$  is the fluctuation of the horizontal velocity), which were not disturbed by frame interference, during periods with low wave energy (wave heights below 0.1 m) and the vertical velocity profile for unstratified channel flow (Dyer and Soulsby 1988):

$$u(z) = \frac{u_*}{\kappa} \ln \left( \frac{z}{z_0} \right), \quad (14)$$

where  $\kappa$  is the van Karmann constant and  $z_0$  is the roughness length. The modal values of  $\log(z_0)$  were  $-4.7$  in spring and  $-3.5$  in fall corresponding to  $z_0 = 2.0 \times 10^{-5}$  m in spring and  $z_0 = 3.4 \times 10^{-4}$  m in fall. The  $\log(z_0)$  values showed a high variability. The 25<sup>th</sup> percentile is  $-5.0$  in spring and  $-4.0$  in fall and the 75<sup>th</sup> percentile was  $-4.3$  in spring and  $-3.2$  in fall. This is most likely due to the fact that the flow is transitional. Using  $u_* = 0.01 \text{ m s}^{-1}$  and the Nikuradse equivalent roughness  $k_s = 30 z_0$  ( $6 \times 10^{-4}$  m in spring and 0.01 m in fall) the wall Reynolds numbers  $Re_w = u_* k_s / \nu$  ( $\nu$  is the kinematic viscosity of water) were



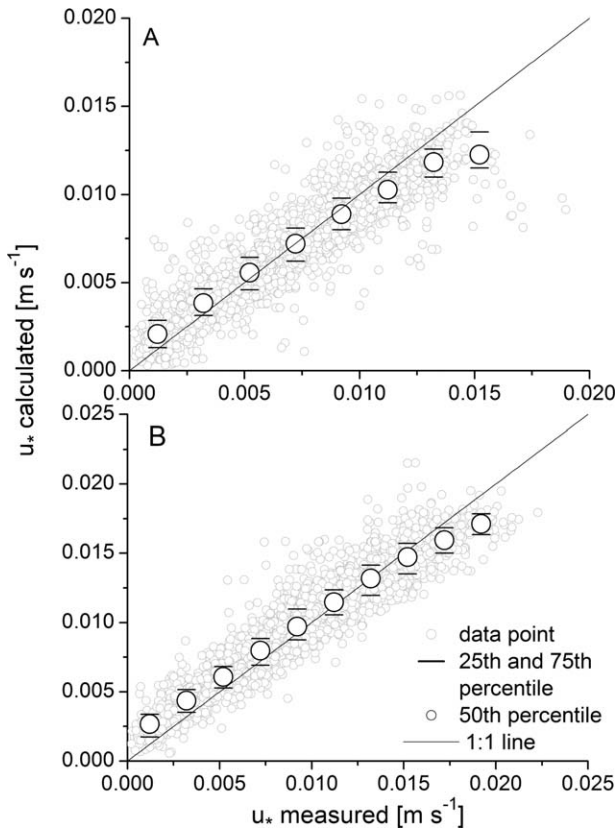


**Fig. 3.** Comparison between measured current shear velocities and those predicted by the Styles and Glenn (2000) model for spring (A) and fall (B).

approximately 6 in spring and 100 in fall, while smooth flows occur when  $Re_w < 3$  and fully rough flows at  $Re_w > 100$ , our observations fell in the range of transitional flow. Analogously to Bricker et al. (2005), we used constant  $z_0$  values ( $2.0 \times 10^{-5}$  m in spring and  $3.4 \times 10^{-4}$  m in fall) as input for the model of Styles and Glenn (2000). As a second step, we used these  $z_0$  values and the horizontal velocities measured at 0.36 m elevation to calculate the characteristic shear velocity due to the current  $u_{*c}$  and the bottom shear stress  $\tau_b$  for the entire dataset using the current wave boundary layer model of Styles and Glenn (2000). The  $u_{*c}$  values obtained from the model were then used to calculate the eddy diffusivities  $\nu_T$  using Eq. 3. In addition to  $z_0$  and mean horizontal current velocity measured at 0.36 m, the Styles and Glenn model requires the wave bottom orbital velocity, wave radian frequency and wave direction. The wave parameters were calculated from the spectra of the velocities determined by the ADV in 0.36 m elevation following Wiberg and Sherwood (2008). The shear velocities predicted by the model were in reasonable agreement with the measured shear velocities (Fig. 3). The slight deviations of the 50<sup>th</sup> percentiles at high shear velocities may be attributed to the fact that the roughness length  $z_0$  can vary

with the bottom stress in San Francisco Bay (Cheng et al. 1999).

### Boundary and initial conditions

As the lower boundary condition at the sediment water interface, we used the difference between bed erosion and deposition  $E-D$ . As the upper boundary condition on top of the water column, we used the zero flux condition. All model runs were initialized with Rouse profiles which matched the observed sediment concentrations at 0.36 m at the beginning of the measurements. Initial concentrations were set to  $7 \text{ g m}^{-3}$  and  $5 \text{ g m}^{-3}$  in spring for the fast settling and slow settling size classes, respectively, and to  $5 \text{ g m}^{-3}$  and  $19 \text{ g m}^{-3}$  in fall. The initial concentration of the slowly settling fraction was estimated by visual inspection of the sediment time series as the amount of sediment in the water column which varied only over the spring-neap cycle and not over the semidiurnal tidal cycle (c.f. Cartwright et al. 2013). The coarse fraction was calculated as the difference between the estimated concentration of the fine fraction and the total sediment concentration.

### Determination of parameters for sediment settling and bed erosion

Various combinations of the sediment settling and sediment bed erosion models were used for the analysis of the recorded time series. In addition to the two particle class model we also tested models which included up to six particle size classes. The inverse fitting routine always converged to two particle size classes with all the other particle class fractions  $\alpha_i$  (Eq. 11) approaching zero (data not shown).

The parameter fitting for the models 1 and 4 (Table 1) was performed by minimizing following objective function:

$$\text{OF} = \sum_n^N (C_{\text{meas},n} - C_{\text{calc},n})^2 + \left( \frac{\sum_n^N C_{\text{meas},n}}{\sum_n^N \overline{w'C'}} \right)^2 \sum_{nl}^N (\overline{w'C'}_{\text{meas},n} - \overline{w'C'}_{\text{calc},n})^2 \quad (15)$$

where  $n$  is the index of the individual measurements,  $N$  the total number of measurements,  $C_{\text{meas},n}$  and  $C_{\text{calc},n}$  the measured and modeled concentrations,  $\overline{w'C'}_{\text{meas},n}$  and  $\overline{w'C'}_{\text{calc},n}$  the measured and modeled turbulent sediment fluxes, where the latter was calculated by

$$\overline{w'C'}_{\text{calc}} = \varepsilon_s \frac{\partial C}{\partial z} \quad (16)$$

The objective function was evaluated with the values measured at 0.36 m. The squared differences of the turbulent sediment fluxes were weighted by the ratio between the average concentration and the average turbulent sediment flux. The average weighting was performed to standardize the magnitudes of both quantities. For the parameter

estimation of the sediment bed models (Eqs. 6-8), we used  $w_{s,slow}$ ,  $w_{s,fast}$ , and  $\alpha$  determined using the flux amplification method (see Table 1). We chose this strategy, since -as we will show later in this manuscript- the flux amplification method provided the best identifiability of the settling parameters for both seasons. In addition, the use of these well-constrained settling parameters also improves significantly the identifiability of the erosion parameters. This is especially an advantage when these parameters are also estimated by minimizing the objective function as we did for the depth-dependent erosion model (Eq. 6). The flux amplification model provided us with parameter-free estimates of the erosion flux. Since the only time-dependent variable of the linear and nonlinear bed erosion models is the bottom shear stress  $\tau_b$ , we were able to determine their parameters by fitting Eqs. 7 and 8 to the erosion fluxes calculated by the flux amplification method directly. Still, this is not possible for the depth-dependent erosion model (Eq. 6), since this model also depends on the eroded mass, which is also a time-dependent variable.

### Assessment of model performance

We evaluated the ability of the various scenarios to reproduce the observed data based on the mean square error (MSE)

$$MSE(f, x) = \frac{1}{N} \sum_n^N (f_n - x_n)^2 \quad (17)$$

where  $x_n$  is the measured value of  $C$ ,  $\overline{w'C'}$ , and  $f_n$  is its prediction by a model, the root mean square error (RMSE),

$$RMSE(f, x) = \sqrt{\frac{1}{N} \sum_n^N (f_n - x_n)^2} \quad (18)$$

and the skill score (SS)

$$SS = \left( 1 - \frac{MSE(f, x)}{MSE(r, x)} \right) \quad (19)$$

where  $r$  is the prediction of a reference model (Murphy and Epstein 1989). As  $r$  we used the average of the quantity  $x_t$  over the observation period.

### Parameter uncertainties, sensitivities and identifiability analysis

All measures for this task were calculated following Brun et al. (2001). The standard deviation of the parameter vector estimated by weighted least squares (WLS)  $\theta_{WLS}$  was calculated as the square root of the diagonal of the covariance matrix

$$VAR(\theta_{WLS}) = \frac{OF}{O - P} (\mathbf{V}^T \mathbf{W} \mathbf{V})^{-1} \quad (20)$$

where  $O$  is the number of observations and  $P$  the number of parameters.  $\mathbf{W}$  is the diagonal matrix of weights and  $\mathbf{V}$  the  $O \times P$  derivative matrix

**Table 1.** Model combinations used for the analysis of the measured concentrations and fluxes.

Erosion model	Parameters fitted
(1) Flux amplification (Eq. 9)	$\alpha_1, \alpha_2, w_{s,fast}, w_{s,slow}, \text{amp}$
(2) Linear erosion model (Eq. 7)	$M, \tau_{crit}$
(3) Non-linear erosion model (Eq. 8)	$M, k$
(4) Depth-dependent erosion model (Eq. 6)	$M_0, \mu, \tau_{crit,0}, \beta$

$$\mathbf{V} = \frac{\partial \eta(\theta)}{\partial \theta^T} \big|_{\theta = \theta_{WLS}} \quad (21)$$

where  $\eta(\theta)$  is the outcome vector of the model evaluated at the same time points as the observations.

The sensitivity analyses were based on the scaled sensitivity matrix  $\mathbf{S} = \{s_{op}\}$  with

$$s_{op} = v_{op} \frac{\Delta \theta_p}{SC_O} \quad (22)$$

where  $v_{op}$  denotes an element of  $\mathbf{V}$ ,  $\Delta \theta_p$  is an a priori measure of the reasonable range of  $\theta_p$  and  $SC_O$  is a scale factor with the same physical dimensions as the corresponding observation. Following Brun et al. (2001), we chose the value of  $\theta_p$  determined from the least squares fitting as  $\Delta \theta_p$  and  $SC_O$  was chosen as 1 when concentrations were considered and  $\sum_n^N C_{meas,n} / \sum_n^N \overline{w'C'}$  when fluxes were considered. As a sensitivity measure for each determined parameter we calculated

$$\delta_p^{msqr} = \sqrt{\sum_o^O s_{op}^2} \quad (23)$$

To assess the identifiability of the various parameters and parameter subsets used in a model scenario it is necessary to calculate the normalized sensitivity matrix  $\tilde{\mathbf{S}}$  with the columns

$$\tilde{\mathbf{s}}_p = \frac{\mathbf{s}_p}{\|\mathbf{s}_p\|} \quad p = 1, 2, \dots, P. \quad (24)$$

From the  $O \times K$  submatrix of  $\tilde{\mathbf{S}}$   $\tilde{\mathbf{S}}_K$ , which contains the columns corresponding to the  $K$  parameters considered in the analysis we can calculate the collinearity index

$$\gamma_K = \frac{1}{\sqrt{\lambda_K}} \quad (25)$$

where  $\lambda_K$  is the smallest eigenvalue of  $\tilde{\mathbf{S}}_K^T \tilde{\mathbf{S}}_K$ . The interpretation of this collinearity index is that a change in one parameter of the set  $K$  can be compensated by up to a factor of  $1/\gamma_K$  by changing all the other parameters in the set. For example, a value of  $\gamma_K$  of 5 means that a change in the output by changing one parameter and be compensated down

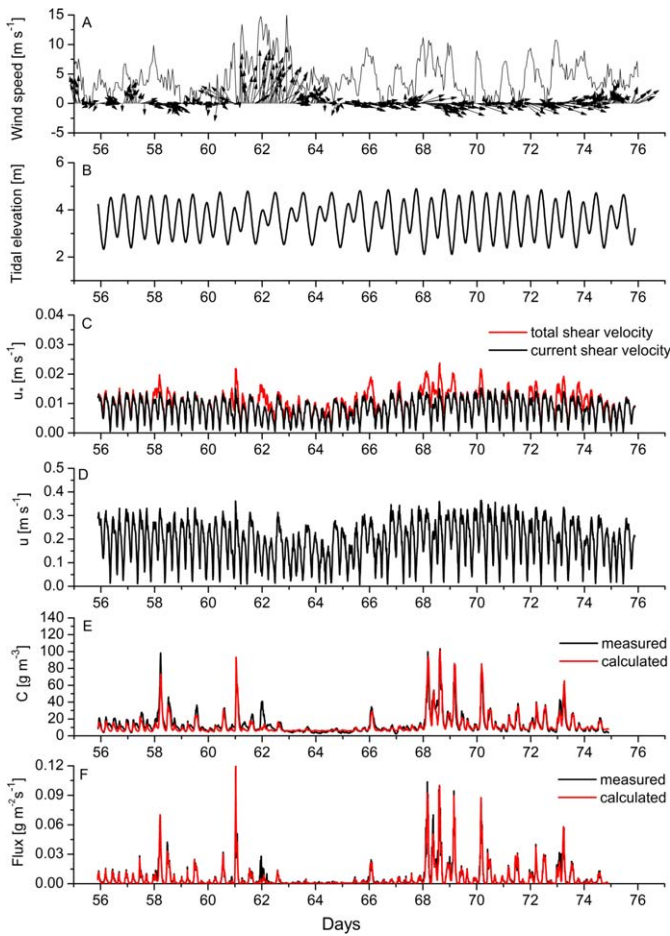


**Fig. 4.** Surrounding conditions during the spring campaign. A) Wind speed and wind direction, B) tidal elevation, C) current and combined current-wave shear stress, D) horizontal velocity 0.36 m above the sediment, E) measured and calculated sediment concentrations, and F) measured and calculated sediment fluxes.

to 20% by changing all other parameters. In general, critical values for identifiability are in the range between 5 and 20.

## Results

### Conditions during the field campaigns

Both field campaigns covered a full spring-neap cycle with phases of low and high tidal energy (Figs. 4B, 5B). During spring, regular winds occurred in the second half of the campaign (starting at day 65) following a storm event between day 60 and 64.5 when wind velocities reached peak values around  $15 \text{ m s}^{-1}$ . Wind velocities were generally lower during spring with maximum velocities around  $10.5 \text{ m s}^{-1}$  and more intermittent than the regular northwesterly winds in fall with peak velocities above  $11 \text{ m s}^{-1}$  (Figs. 4A, 5A).

Horizontal flow velocities measured at 0.36 m were similar during both campaigns with maximum tidal velocities around  $0.15\text{--}0.20 \text{ m s}^{-1}$  at periods with low tidal energy

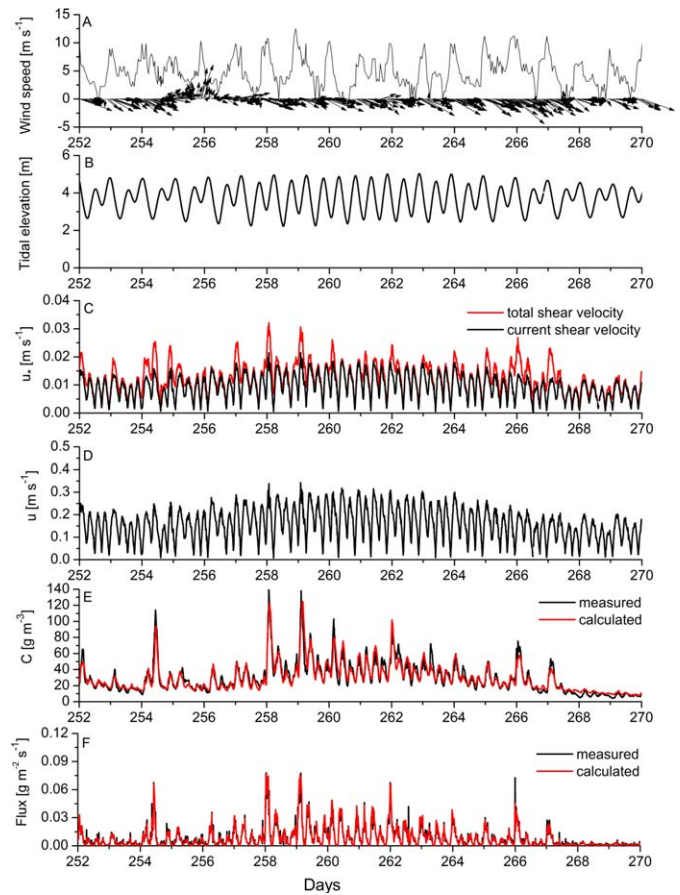


**Fig. 5.** Surrounding conditions during the fall campaign. A) Wind speed and wind direction, B) tidal elevation, C) current and combined current-wave shear stress, D) horizontal velocity at 0.36 m above the sediment, E) measured and calculated sediment concentrations, and F) measured and calculated sediment fluxes.

(days 63–66 during spring and days 252–257 and 266–270 during fall) and maximum velocities around  $0.3 \text{ m s}^{-1}$  during periods with high tidal energy (days 56–63 and 66–76 in spring and days 257–266 in fall) (Figs. 4D, 5D). Still, current induced shear velocities were significantly higher during fall with peak values between  $0.017 \text{ m s}^{-1}$  and  $0.019 \text{ m s}^{-1}$  as compared to values around  $0.014 \text{ m s}^{-1}$  during spring due to an increase of bed roughness height ( $z_0$  was determined from modal logarithmic values was  $3.4 \times 10^{-4} \text{ m}$  in fall and  $2.8 \times 10^{-5} \text{ m}$  in spring). During both periods, wind induced waves resulted in an increase of bottom shear velocity of more than  $0.01 \text{ m s}^{-1}$  compared to  $u_{*c}$  in the absence of waves (e.g., days 62, 66, and 67.5–70.2 in spring and days 254–255, 257–260, and 266–268 in fall; Figs. 4C, 5C). The increased bottom stresses resulted in a significant enhancement of turbulent sediment fluxes during the periods of high current velocities and high sediment concentrations in the water (Figs. 4F, 5F). It is interesting to note that the peak concentrations during the spring campaign (around  $100 \text{ g}$

$\text{m}^{-3}$  during days 68.6, 68.2, and 58.2) were significantly lower than the peak concentrations during fall (around  $140 \text{ g m}^{-3}$  during days 258 and 259; Figs. 4E, 5E), even though the corresponding turbulent sediment fluxes were

higher in spring (around  $0.1 \text{ g m}^2 \text{ s}^{-1}$ ) than in fall (around  $0.07 \text{ g m}^2 \text{ s}^{-1}$ ).

## Modeling

### Suspended particle properties

We used the two particle class model and the flux amplification model to describe the sediment concentrations and turbulent sediment fluxes observed at 0.36 m above the sediment bed in spring and fall. Parameter values determined by fitting and their standard deviations as well as model performance measures are presented in Table 2. The model results reproduced the measured concentrations and turbulent sediment fluxes reasonably well (Figs. 4E,F, 5E,F, 6). Turbulent sediment fluxes were reproduced extremely well ( $SS > 0.97$ ). The predicted concentrations were more scattered ( $SS = 0.83$  for spring and  $SS = 0.88$  for fall), and the model underestimated the peak concentrations during fall slightly (Fig. 5E). The concentrations at 0.72 m were also adequately described ( $SS = 0.74$  for spring and  $0.86$  for fall and Fig. 7A, C) while the fluxes were slightly overestimated ( $SS 0.26$  for spring and  $0.61$  for fall and Fig. 7B, D). Still, the model predictions were in good agreement with the measurement considering that data recorded at 0.72 m were not included in the objective function (Eq. 15).

The model predicted a seasonal variation in the particle properties (Fig. 8). The fast settling flocs contributed mainly to the variability of sediment concentration over the semidiurnal tidal cycle. The settling velocity  $w_{s,\text{fast}}$  predicted by the model

**Table 2.** Fitted parameters for the flux amplification method and model performance parameters for  $C$  and  $w'C'$  at 0.36 m and 0.72 m elevation.

	Spring	Fall
amp [-]	$1.72 \pm 0.01$	$1.4 \pm 0.01$
$\alpha$ [-]	$4.7 \times 10^{-4} \pm 2.2 \times 10^{-4}$	$1.5 \times 10^{-2} \pm 6.6 \times 10^{-4}$
$w_{s,\text{fast}}$ [ $\text{m s}^{-1}$ ]	$9.0 \times 10^{-4} \pm 1 \times 10^{-5}$	$5.8 \times 10^{-4} \pm 1 \times 10^{-5}$
$w_{s,\text{slow}}$ [ $\text{m s}^{-1}$ ]	$1.0 \times 10^{-7} \pm 4.0 \times 10^{-7}$	$1.4 \times 10^{-5} \pm 5.0 \times 10^{-7}$
$SS \bar{w'C'}$ 0.36 m	0.97	0.98
RMSE $\bar{w'C'}$	$2.1 \times 10^{-3}$	$1.7 \times 10^{-3}$
[ $\text{g m}^{-2} \text{ s}^{-1}$ ] 0.36 m		
$SS C$ 0.36 m	0.83	0.88
RMSE $C$	5.1	6.5
[ $\text{g m}^{-3}$ ] 0.36 m		
$SS \bar{w'C'}$ 0.72 m	0.26	0.61
RMSE $\bar{w'C'}$	$5.6 \times 10^{-3}$	$4.8 \times 10^{-3}$
[ $\text{g m}^{-2} \text{ s}^{-1}$ ] 0.72 m		
$SS C$ 0.72 m	0.74	0.86
RMSE $C$	4.6	6.2
[ $\text{g m}^{-3}$ ] 0.72 m		

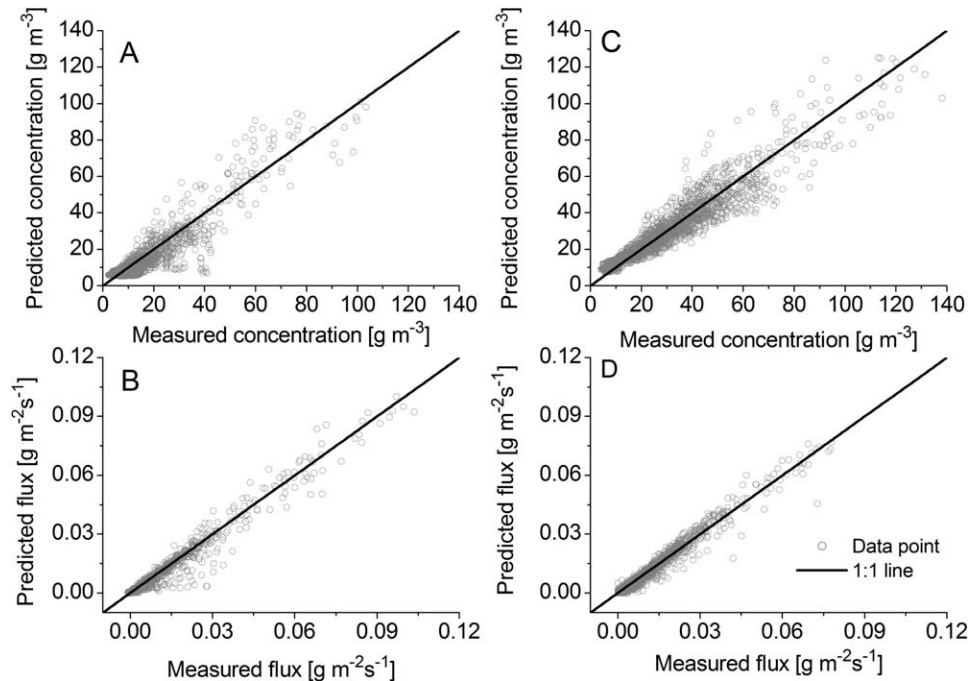


**Fig. 6.** Comparison between measured and modeled sediment concentrations and sediment fluxes at 0.36 m elevation using the flux amplification method A) concentration spring, B) flux spring, C) concentration fall, and D) flux fall.



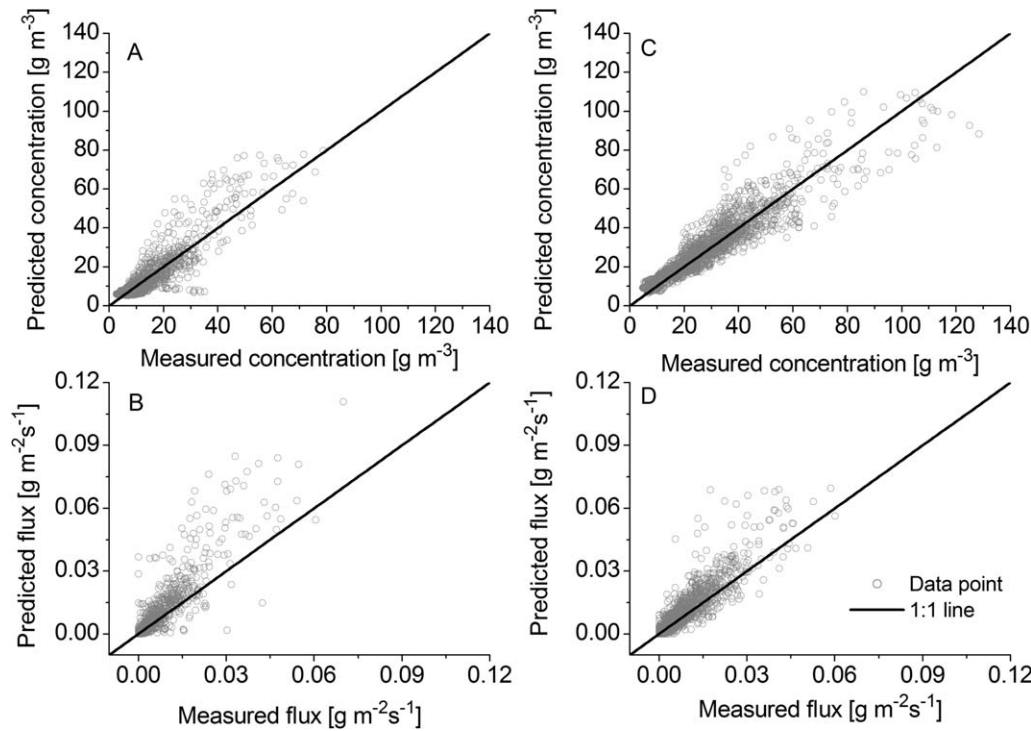


**Fig. 7.** Comparison between measured and modeled sediment concentrations and sediment fluxes at 0.72 m elevation using the flux amplification method. A) Concentration spring, B) flux spring, C) concentration fall, and D) flux fall.

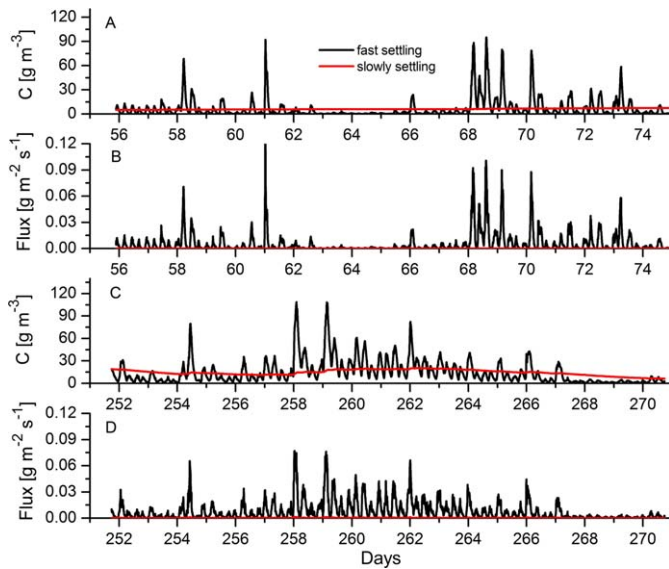


**Fig. 8.** Contribution of slowly settling sediment and fast settling sediment to concentrations and vertical turbulent fluxes  $\overline{wC'}$ . A) concentration spring, B) flux spring, C) concentration fall, and D) flux fall.

was higher during spring ( $9.0 \times 10^{-4} \text{ m s}^{-1}$ ) than during fall ( $5.8 \times 10^{-4} \text{ m s}^{-1}$ ). In addition, the contribution of the slowly settling sediment to the overall sediment dynamics was greater in fall (Fig. 8C). The calculated fine sediment fraction  $\alpha_2$  in

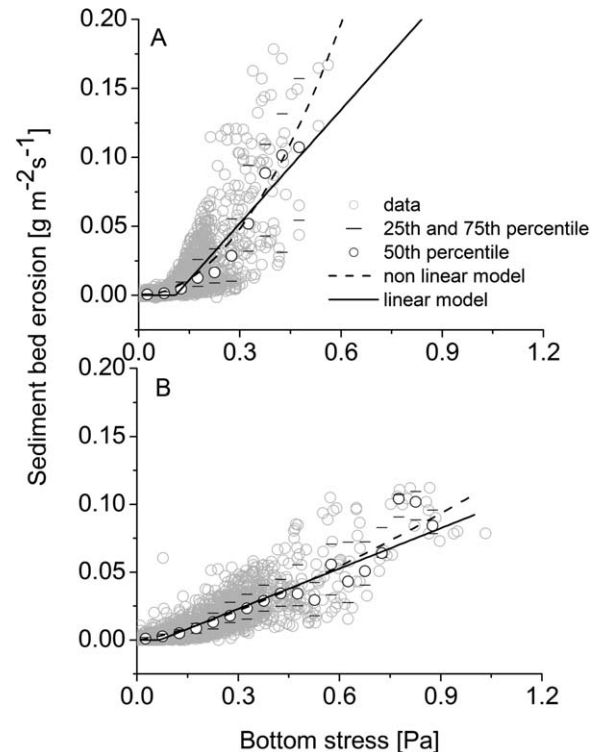


**Fig. 9.** Sediment bed erosion as function of bottom shear stress during A) spring and B) fall in comparison with the linear erosion model (Eq. 7) and the nonlinear erosion model (Eq. 8).

**Table 3.** Parameters of the depth-dependent bed erosion model (Eq. 6), the linear bed erosion model (Eq. 8), and model performance parameters.  $M$ ,  $\tau_{crit}$  and  $k$  were determined by fitting the bed erosion models to erosion fluxes calculated by the flux amplification method as functions of the bottom shear stress. All parameters for the depth-dependent erosion model (Eq. 6) were determined by minimizing the objective function (Eq. 15)

	Linear erosion model		Nonlinear erosion model		Depth-dependent erosion model	
	Spring	Fall	Spring	Fall	Spring	Fall
$M$ [ $\text{g m}^{-2} \text{s}^{-1} \text{Pa}^{-1}$ ]	$0.274 \pm 0.07$	$0.099 \pm 0.001$	$0.552 \pm 0.203$	$0.113 \pm 0.016$	—	—
$\tau_{crit}$ [Pa]	$1.1 \times 10^{-1} \pm 1.8 \times 10^{-3}$	$6.8 \times 10^{-2} \pm 2.8 \times 10^{-3}$	—	—	—	—
$k$	—	—	$2.03 \pm 0.06$	$1.33 \pm 0.03$	—	—
$M_0$ [ $\text{g m}^{-2} \text{s}^{-1} \text{Pa}^{-1}$ ]	—	—	—	—	$0.102 \pm 0.006$	$0.101 \pm 0.002$
$\mu$ [ $\text{m}^{-2} \text{s}^{-1} \text{Pa}^{-1}$ ]	—	—	—	—	$2.4 \times 10^{-3} \pm 0.1 \times 10^{-3}$	$6.7 \times 10^{-5} \pm 1.5 \times 10^{-5}$
$\tau_{crit,0}$ [Pa]	—	—	—	—	$4.7 \times 10^{-2} \pm 0.4 \times 10^{-2}$	$6.7 \times 10^{-2} \pm 3.7 \times 10^{-3}$
$\beta$ [ $\text{Pa g}^{-1}$ ]	—	—	—	—	$6.5 \times 10^{-4} \pm 0.5 \times 10^{-4}$	$2.4 \times 10^{-10} \pm 6.1 \times 10^{-5}$
$SS \overline{wC'}$	$0.63$	$0.77$	$0.63$	$0.77$	$0.70$	$0.76$
$RMSE \overline{wC'}$ [ $\text{g m}^{-2} \text{s}^{-1}$ ]	$7.7 \times 10^{-3}$	$5.2 \times 10^{-3}$	$7.8 \times 10^{-3}$	$5.2 \times 10^{-3}$	$6.8 \times 10^{-3}$	$5.3 \times 10^{-3}$
$SS C$	$0.63$	$0.81$	$0.65$	$0.80$	$0.66$	$0.83$
$RMSE C$ [ $\text{g m}^{-3}$ ]	$7.7$	$8.5$	$7.4$	$8.5$	$7.4$	$8.0$
$SS \overline{wC'} 0.72 \text{ m}$	$0.19$	$0.56$	$0.16$	$0.54$	$0.14$	$0.44$
$RMSE \overline{wC'}$ [ $\text{g m}^{-2} \text{s}^{-1}$ ] $0.72 \text{ m}$	$5.1 \times 10^{-3}$	$6.0 \times 10^{-3}$	$5.2 \times 10^{-3}$	$5.8 \times 10^{-3}$	$6.1 \times 10^{-3}$	$5.8 \times 10^{-3}$
$SS C 0.72 \text{ m}$	$0.64$	$0.82$	$0.65$	$0.83$	$0.62$	$0.82$
$RMSE C$ [ $\text{g m}^{-3}$ ] $0.72 \text{ m}$	$5.4$	$6.9$	$5.3$	$6.9$	$5.6$	$7.02$

the bed sediment during fall was 1.5% while fine sediment was virtually absent in the bed sediments during spring ( $\alpha_2 = 0.05\%$ ). During spring, the model predicted an almost constant fine sediment concentration of  $6 \text{ g m}^{-3}$  throughout the campaign which did not settle out (the fitted value  $w_{s,slow} = 1.0 \times 10^{-7} \text{ m s}^{-1}$  was the lower limit set for the fitting routine; Fig. 8C). In fall,  $w_{s,slow}$  was significantly higher ( $1.4 \times 10^{-5} \text{ m s}^{-1}$ ) and the fine sediment concentration followed the spring-neap cycle with concentrations of up to  $20 \text{ g m}^{-3}$  during periods of high tidal energy and concentrations between  $6 \text{ g m}^{-3}$  and  $10 \text{ g m}^{-3}$  during periods of low tidal energy (Fig. 8A). As the profiles of the slowly settling particles did not form steep gradients, their contribution to the observed turbulent sediment flux was negligible compared to the contribution of the fast settling particles during both seasons (Fig. 8B, D; c.f., Cartwright et al. 2013).

#### Sediment bed erosion model

In general, we observed a higher sediment erodibility for a given shear stress in spring than in fall (Fig. 9). This is reflected by the higher  $M$  value in spring for the linear erosion model in spring ( $0.274 \text{ g m}^{-2} \text{s}^{-1} \text{Pa}^{-1}$ ) compared to fall ( $0.099 \text{ g m}^{-2} \text{s}^{-1} \text{Pa}^{-1}$ ) while the critical shear stresses are comparable ( $1.1 \times 10^{-1} \text{ Pa}$  in spring and  $6.8 \times 10^{-2} \text{ Pa}$  in fall). The nonlinear erosion model describes the same trend. Still, the parameters  $M$  and  $k$  of the nonlinear model cannot be directly compared between different seasons, as both parameters are tightly coupled as we will show in the discussion on the identifiability analysis. Both models provide equally good data prediction (see RMSE and SS in Table 3). The calculated concentrations and turbulent sediment fluxes reproduced the observed trends reasonably well (Fig. 10 and SS in Table 3), although the model skill for concentrations and turbulent sediment fluxes was lower compared to the flux amplification method and in particular, high concentration peaks (e.g., during days 68–69 in spring and at day 254.42 and 258.06 in fall) were less well reproduced (Figs. 6, 11). The depth-dependent erosion model (Eq. 6) did not improve the model performance compared to the other two models (see SS and RMSE values in Table 3). The fact that we did not include settling velocities as fitting parameters when we determined sediment bed properties as well as the fact that we did not minimize the objective function (Eq. 15) when we determined the erosion parameters of the models 2 and 3 does not affect our conclusions in this chapter. We tested this by performing a full parameter fit for the depth-dependent and the linear erosion models in fall by minimizing equation 15. All RMSE and SS values improved by less than 10% while the change in parameters was negligible. In fall, the critical shear stress  $\tau_{crit}(m_R)$  varies only slightly from  $6.7 \times 10^{-2} \text{ Pa}$  to  $7.0 \times 10^{-2} \text{ Pa}$  and  $M(m_R)$  from  $0.101 \text{ g m}^{-2} \text{s}^{-1} \text{Pa}^{-1}$  to  $0.122 \text{ g m}^{-2} \text{s}^{-1} \text{Pa}^{-1}$ , which is very similar to the parameters obtained for the linear erosion model. In spring, the values range for  $\tau_{crit}(m_R)$  from

$4.67 \times 10^{-2}$  Pa to  $1.77 \times 10^{-1}$  Pa and for  $M$  from  $0.102 \text{ g m}^{-2} \text{ s}^{-1} \text{ Pa}^{-1}$  to  $0.574 \text{ g m}^{-2} \text{ s}^{-1} \text{ Pa}^{-1}$ . The values of the linear erosion model are in the middle of this range.

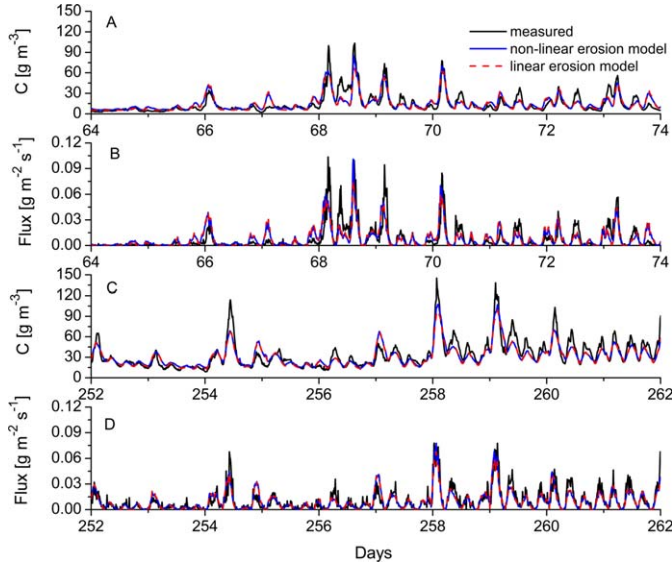


**Fig. 10.** Comparison between measured time series and modeled time series based on the linear bed erosion model and the nonlinear bed erosion model. A) Sediment concentrations spring, B) Reynolds sediment fluxes ( $\overline{w'C'}$ ) spring, C) sediment concentrations fall, and D) Reynolds sediment fluxes ( $\overline{w'C'}$ ) fall.

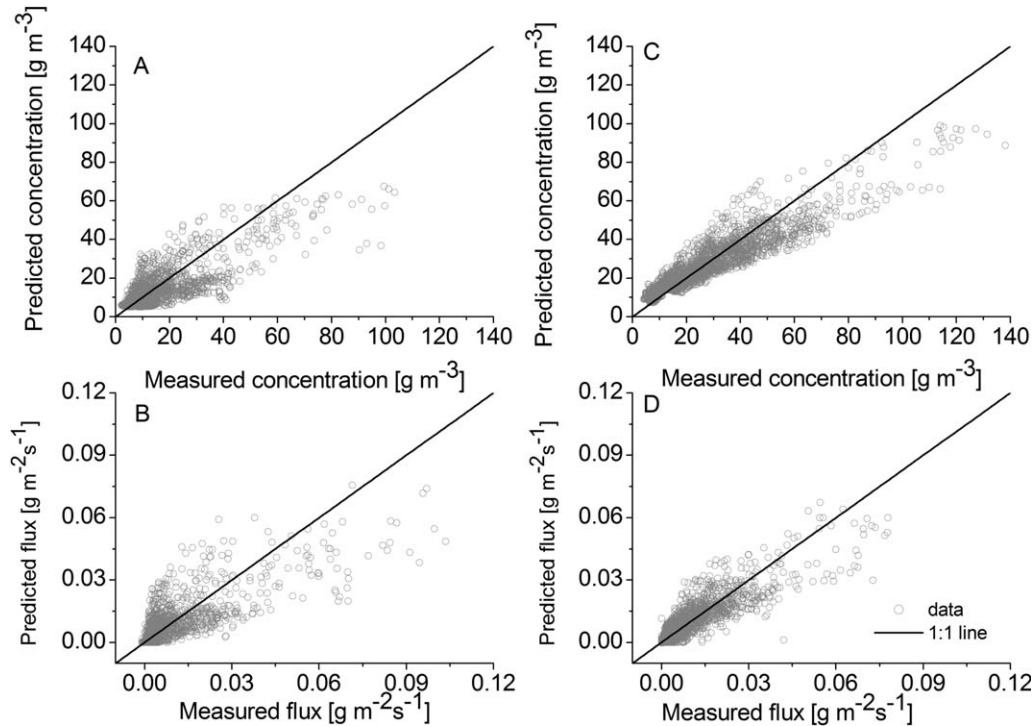


**Fig. 11.** Comparison between measured and modeled sediment concentrations and sediment fluxes based on the linear erosion model. A) concentration spring, B)  $\overline{w'C'}$  spring, C) concentration fall, and D)  $\overline{w'C'}$  fall.

## Discussion

### Transport and mixing model

#### Influence of horizontal flux convergence

To investigate whether the concentration change over time in the water column was dominated by local resuspension and settling dynamics, we estimated the cross channel horizontal flux convergence based on the sediment concentration gradients between Sh and Be station (Fig. 1). As Brand et al. (2010) pointed out, the along channel sediment

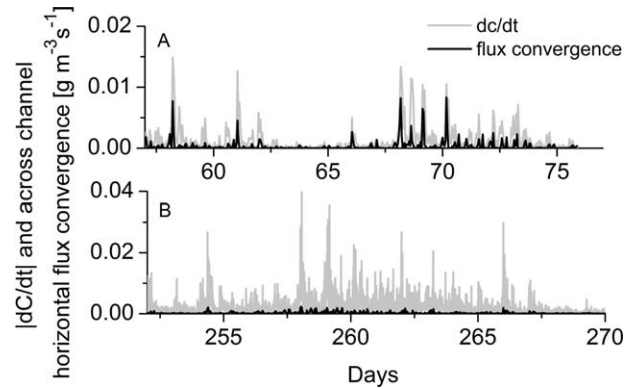


**Fig. 12.** Concentration change over time during spring (A) and fall (B) in comparison with the estimated cross channel flux convergence. The cross channel concentration gradient  $dC/dx$  was calculated from the measurements between Be and Sh.

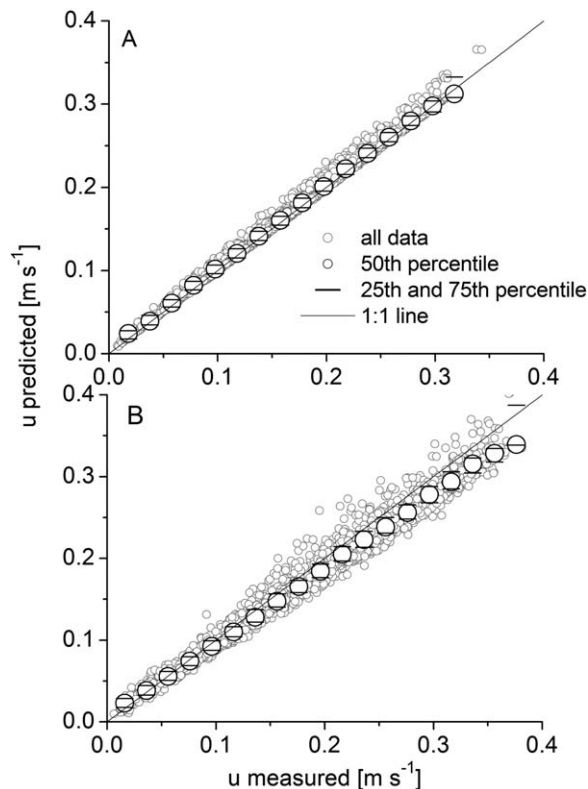


**Fig. 13.** Comparison between the horizontal velocity measured in fall at A) 0.36 m and B) 0.72 m and those predicted by the parabolic law. The characteristic shear velocity  $u_{*c}$  calculated by Styles and Glenn (2000) was used as the shear velocity.

concentration gradient at our field site was negligible compared to the cross channel variation and we expected the larger contribution of change in concentration over time from the cross channel flux convergence. Figure 12 compares the cross channel flux convergence with the change in concentration over time determined from the data. Besides three single events in spring at days 68.1, 69.3, and 70.2, the concentration change over time was significantly larger than the estimated cross channel flux convergence. The measured average concentration change over time was four times the average horizontal cross channel flux convergence in spring and 14 times in fall. Lacy et al. (2014) pointed out that the measured horizontal concentration cross channel gradients may even overestimate the local horizontal cross channel concentration gradients at Be, where the bathymetry is very uniform. Therefore, neglecting horizontal flux convergence was a reasonable approximation.

#### *Influence of stratification*

Many studies on estuarine mixing and sediment dynamics have shown that sediment induced stratification can strongly influence vertical mixing (Wiberg et al. 1994, Sherwood et al. 2006). In San Francisco Bay, a significant influence of sediment induced stratification has been found in

the very shallow parts of the northern San Francisco Bay (MacVean and Lacy 2014) and at this site during very strong wind events (Lacy et al. 2014). To assess the influence of density stratification, we included the stratification correction for the eddy diffusivity based on the Monin–Obukov length following Styles and Glenn (2000) and Wiberg and Smith (1983). Two conductivity sensors which were mounted on the Be station did not detect any vertical salinity gradient. Therefore, we restricted our model study to sediment induced stratification. The changes due to the inclusion of sediment stratification on the model results are negligible under the observed conditions at the Be site (data not shown).

#### *Modeling the influence of waves on bottom shear and vertical mixing*

We used the formulation of Styles and Glenn (2000) to calculate the combined current-wave shear stress. Turbulence in the wave boundary layer increases the near-bed current shear  $u_{*c}$ . This aspect was accounted for in our model based on the formulation of Styles and Glenn (2000). The good agreement between the horizontal velocities measured at 0.36 m and 0.72 m with those predicted using the parabolic mixing model (Fig. 13) is consistent with the use of our modeling approach.

#### *Particle dynamics*

The model results based on two different particle populations with constant settling velocities suggested one population which was settling out over the diurnal tidal cycle, while concentration of the other population was almost constant in spring and varied over the spring-neap cycle in fall. Similar observations were reported by Kranck and Milligan (1992) and by Cartwright et al. (2013), who observed the existence of two particle size classes in studies in San Pablo Strait and in the York River estuary, respectively. They both found that larger flocs were stable and resuspended and settled out without much floc breakup. In addition to these larger flocs, a stable background concentration of small flocs was observed. The small flocs had sufficiently low settling rates to remain in suspension over the whole semidiurnal tidal cycle while the other particle population was alternately settling and resuspending over the semidiurnal tidal cycle. In our campaign, we calculated settling velocities of the fast settling fraction of  $9.0 \times 10^{-4} \text{ m s}^{-1}$  in spring and  $5.8 \times 10^{-4} \text{ m s}^{-1}$  in fall. These values were significantly lower than those reported by Manning et al. (2010) ( $4\text{--}8 \times 10^{-3} \text{ m s}^{-1}$ ) and Sternberg et al. (1986) ( $2.8 \times 10^{-3} \text{ m s}^{-1}$ ) in the Central San Francisco Bay, but were in the range reported by Kineke et al. (1989) of  $2 \times 10^{-4} \text{ m s}^{-1}$  to  $2.5 \times 10^{-3} \text{ m s}^{-1}$  from a field campaign in San Pablo Bay and also in the range reported by Cartwright et al. (2013) of  $3 \times 10^{-4} \text{ m s}^{-1}$  to  $7 \times 10^{-4} \text{ m s}^{-1}$  for the fast settling component for flocs in the York River estuary.

Particle settling velocities can be estimated from ADV measurements when a Rouse balance holds using the



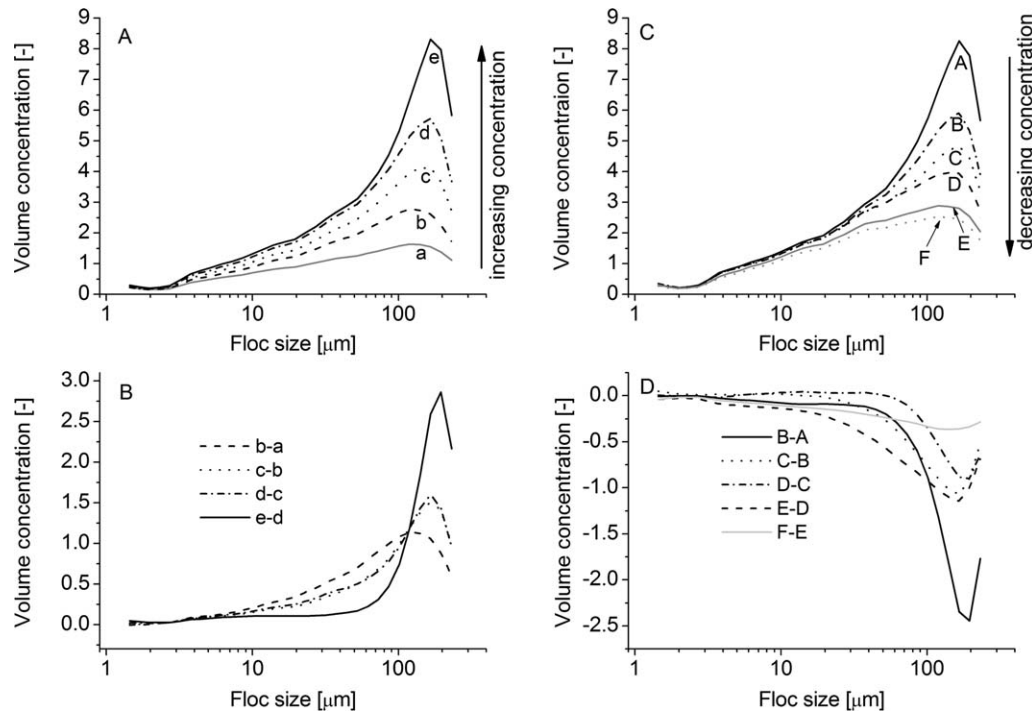


**Fig. 14.** Size distribution dynamics of suspended flocs determined by the LISST between day 257.8 and 257.40 in 36-min intervals. A) Floc size distributions during period of increasing sediment concentration. B) Difference between the subsequent particle-size distributions during period of increasing sediment concentration. C) Floc size distribution during period of decreasing concentration. D) Difference between the subsequent particle-size distributions during period of decreasing sediment concentration.

relationship  $\overline{w'C'} = w_s C$ , as a calibrated ADV can directly measure both  $\overline{w'C'}$  and  $C$  (Fugate and Friedrichs 2002). However, application and interpretation of the resulting value for  $w_s$  depends on one's conceptual model for the structure of the overall population of suspended sediment. For example, Ha and Maa (2010) assumed that the characteristic settling velocity for a suspension of fine sediment should increase with sediment concentration because of an increase in floc size due to a higher collision frequency between flocs (c.f., Pejrup and Mikkelsen 2010). Thus Ha and Maa (2010) fit the relationship  $\overline{w'C'} = aC^q$  to ADV lab observations of suspended mud and argued that  $w_s = aC^{q-1}$ , under the assumption that the higher fraction of fast settling particles results in an increase of the observed (bulk) settling velocity. In contrast, Cartwright et al. (2013) assumed that an ADV deployed in situ in the York River estuary was responding mainly to two noninteracting particle classes which settle out with two different settling velocities ( $w_{s,slow}$  and  $w_{s,fast}$ ), such that  $C = C_{fast} + C_{slow}$ . Cartwright et al. (2013) argued that only  $C_{fast}$  contributed notably to  $\overline{w'C'}$ , so that as observed by the ADV  $w_{s,fast} = \overline{w'C'}/C_{fast}$ . Cartwright et al. (2013) set  $C_{slow}$  equal to the lowest value for  $C$  observed over the semidiurnal tidal cycle and defined  $C_{fast} = C - C_{slow}$ . The approach of Cartwright et al. (2013) is consistent with the water column model favored in this article and also corresponds closely to the observations reported by Kranck and Milligan (1992),

that is, that flocs were resuspended and settled out without much breakup while the smaller particles stayed in suspension. Using our observations, we tested both the concentration-dependent  $w_s$  approach of Ha and Maa (2010) and the noninteracting particle classes' approach of Cartwright et al. (2013). Statistically, they both provided similarly good fits to observed total concentration. Using the Ha and Maa (2010) approach, the best-fit was  $a = 1.5 \times 10^{-4}$  and  $q = 1.43$  in spring and  $a = 5.0 \times 10^{-5}$  and  $q = 1.51$  in fall (data not shown). The main reason why both approaches provided similar good fits is their ability to predict a decreasing settling velocity with decreasing sediment concentration. As we will show in the next paragraphs, a detailed analysis of a resuspension event in fall using LISST particle-size distributions (Fig. 14) suggested that a separate particle size class model is the physically valid approach at our field site.

The data were recorded during an ebb on day 257.1–257.45, with a peak Reynolds stress of  $3 \times 10^{-4} \text{ m}^2 \text{ s}^{-2}$  (Fig. 15B). The suspended sediment concentration determined by the ADV increased from  $10 \text{ g m}^{-3}$  to  $45 \text{ g m}^{-3}$  (Fig. 15C). At the beginning of the period of increasing concentration, a noticeable increase in fine particles ( $<100 \mu\text{m}$ ) was observed in addition to a moderate increase of coarser particles ( $>100 \mu\text{m}$ ) (see difference spectra b-a, c-b, and d-c in Fig. 14B). Just before the sediment concentration maximum the increase in concentration was mainly due to coarse flocs, and the

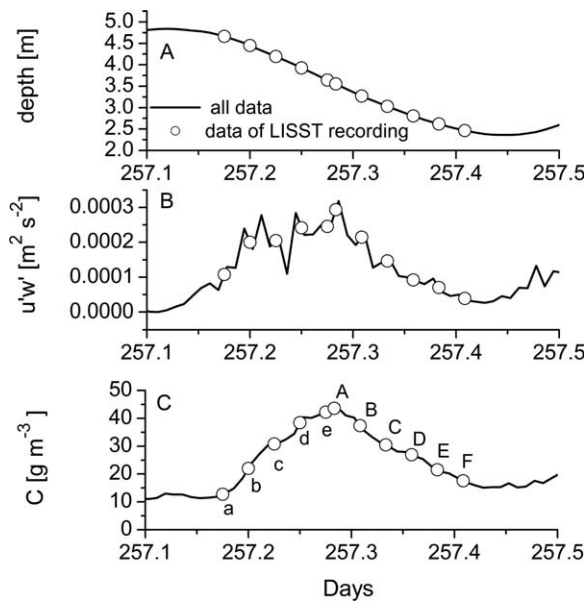


**Fig. 15.** Environmental conditions during the recording of the LISST data shown in Figure 14. A) Tidal elevation, B) Reynolds stress, and C) sediment concentration determined from the ADV backscatter.

amount of fine particles stayed constant (Fig. 14B, difference spectrum e-d). The change of the particle-size distribution during the period of decreasing sediment concentration followed the opposite sequence, beginning with a strong decrease of coarse particles (difference spectrum B-A, Fig. 14D). The decrease in sediment concentration due to coarse particles slowed down gradually and the contribution of fine particles in the settling fraction increased (Fig. 14D, difference spectrum E-D). If coagulation was an important mechanism, coarse particles would grow at the expense of finer particles. Such a mechanism would be indicated by negative values for fine particles in the difference spectra during periods of resuspension, which was not observed (Fig. 14B, difference spectrum e-d). Also, during the periods of high, almost constant sediment concentrations (days 257.27 and 257.28, Fig. 15C) the particle-size distributions were almost identical (spectra e and A in Fig. 14A, C) and did not show an increase of coarse particles at the expense of fine particles.

It is most likely that the observed particle-size distributions reflected resuspension of larger sediment flocs with increasing bottom shear stress and the influence of particle size on the ability of turbulence to mix flocs up to the measurement volume of the LISST 0.55 m above the sediment bed. Apparently, the fraction of finer flocs was greater at the beginning of the sediment resuspension, and the contribution of coarser flocs increased with increasing shear velocity. This was most likely due to the fact that lower turbulence could only resuspend small flocs from the bed at the beginning of the bed erosion period. Over time, the sediment became depleted of small flocs, and only coarser particles

were resuspended as turbulence increased (Van Prooijen and Winterwerp 2010). During the period of decreasing sediment concentration, decreasing turbulence was no longer able to mix coarse particles to the observation elevation and with further decrease of turbulence, finer particles also settled out. This mechanism of resuspending increasingly larger particles from the bed sediment has also been proposed by Fugate and Friedrichs (2002) based on their LISST measurements at a field site in Chesapeake Bay. In addition, they also found that the use of constant settling velocities described their data sufficiently well (Fugate and Friedrichs 2002). Similar to our study, sediment concentrations at their field site were relatively low ( $<60 \text{ g m}^{-3}$  0.25 m above sediment bed). Apparently, sediment flocculation in the water column is not significant at low sediment concentrations, as the collision frequency between flocs is low. Our LISST data suggested the existence of more than one particle size class with semidiurnal variation in concentration. However, the inclusion of only one fast settling particle size class prove to be sufficient to reproduce concentrations and turbulent sediment fluxes obtained by the ADVs and the use of additional particle size classes did not improve the model performance. This suggests that ADV concentration and flux measurements provide coarse bulk properties of the suspended sediment rather than a detailed picture of resuspension and settling dynamics.

The use of a constant fine particle fraction  $\alpha_2$  did not necessarily reflect the exact bed sediment properties. Still, our approach allowed inferring the origin and nature of the slowly settling particles. The  $w_s$  of the slowly settling particle fraction was significantly lower during the spring campaign than during fall and was characterized by very slow settling velocities providing a rather constant background concentration. A likely source of such particles during spring might have been plankton which was not subject to settling. In contrast, the modeled concentration of the slowly settling particle fraction in fall varied significantly over the spring-neap cycle while it did not change over the semidiurnal tidal cycle (Fig. 8). Particle size estimates for the slowly settling fraction with a settling velocity  $w_{s,\text{slow}}$  of  $1.4 \times 10^{-5} \text{ m s}^{-1}$  based on Stoke's law (Winterwerp and van Kesteren 2004) using a particle density of  $2650 \text{ kg m}^{-3}$  resulted in a grain size of  $4 \mu\text{m}$ . A maximum in the particle-size distribution of the disaggregated sediment was observed between  $4 \mu\text{m}$  and  $5 \mu\text{m}$  (see Fig. 3 in Brand et al. 2010), suggesting that the slowly settling particle fraction in fall consisted of single grains. The distributions during both campaigns were almost identical with a modal value of  $9 \mu\text{m}$  and 25 and 75 percentiles at  $3 \mu\text{m}$  and  $30 \mu\text{m}$  related to volume concentrations.

#### Model assessment based on sensitivity and identifiability analysis

The results of the sensitivity analysis are given in Table 4. While all of the models are quite sensitive to the fast settling

**Table 4.** Sensitivity measure  $\delta^{\text{msqr}}$  of the individual parameters for the different model approaches

	Flux amplification		Linear erosion model		Nonlinear erosion model		Depth-dependent erosion model	
	Spring	Fall	Spring	Fall	Spring	Fall	Spring	Fall
amp [-]	15	26	—	—	—	—	—	—
$\alpha$ [-]	0.92	9.3	0.87	8.7	0.97	8.9	0.99	9.3
$w_{s,\text{fast}}$ [ $\text{m s}^{-1}$ ]	14	18	12	17	13	17	21	20
$w_{s,\text{slow}}$ [ $\text{m s}^{-1}$ ]	0.11	9.6	0.11	9.0	0.11	9.3	0.11	9.6
$M$ [ $\text{g m}^{-2} \text{s}^{-1} (\text{Pa})^{-k}$ ]	—	—	12	24	13	25	—	—
$\tau_{\text{crit}}$ [Pa]	—	—	12	8.5	—	—	—	—
$k$	—	—	—	—	142	202	—	—
$M_0$ [ $\text{g m}^{-2} \text{s}^{-1} \text{Pa}^{-1}$ ]	—	—	—	—	—	—	9.12	26
$\mu$ [ $\text{m}^{-2} \text{s}^{-1} \text{Pa}^{-1}$ ]	—	—	—	—	—	—	12	2
$\tau_{\text{crit},0}$ [Pa]	—	—	—	—	—	—	5.3	9.2
$\beta$ [ $\text{Pa g}^{-1}$ ]	—	—	—	—	—	—	5.4	$2.2 \times 10^{-7}$

velocity  $w_{s,\text{fast}}$  during both seasons ( $\delta^{\text{msqr}} = 12\text{--}21$ ), the model is only sensitive to the parameters of the slowly settling fraction during fall, when the fine particle content and the settling velocities are higher. The sensitivities of  $M$  and  $\tau_{\text{crit}}$  range for the linear erosion model during both seasons between 8.5 and 24 and the model results are similarly sensitive to these parameters as the fast settling velocities. The nonlinear erosion model is extremely sensitive to a change in the exponent  $k$  ( $\delta^{\text{msqr}} = 142\text{--}202$ ). In Fall, the model results are quite sensitive to  $M_0$  and  $\tau_{\text{crit},0}$  ( $\delta^{\text{msqr}}$  is 26 and 9.2, respectively) while the coefficients  $\mu$  and  $\beta$  have a low sensitivity on the model results ( $\delta^{\text{msqr}}$  is 2 and  $2.2 \times 10^{-7}$ ), respectively.  $\delta^{\text{msqr}}$  of the parameters describing a depth-dependent  $\tau_{\text{crit}}$  in spring are also relatively low (5.3 for  $\tau_{\text{crit},0}$  and 5.4 for  $\beta$ ) while  $\delta^{\text{msqr}}$  for  $M_0$  and  $\mu$  are relatively high.

The flux amplification method gives the best identifiability (indicated by the smallest  $\gamma_K$ ) of the full parameter set while the identifiability is better in fall compared to spring (Table 5). This is mainly due to the coupling between  $\alpha$  and  $w_{s,\text{slow}}$ . If either of the parameters is removed,  $\gamma_K$  for the remaining subset drops below 3 indicating a very good identifiability of the remaining parameters. The nonlinear erosion model is by far the least identifiable one.  $\gamma_K$  values of the erosion parameter set of 50 and 36 in spring and fall, respectively, indicate that a change in  $M$  or  $k$  can be compensated down to 2% and 3% by changing the second parameter (Table 5). The identifiability of the erosion parameters of the depth-dependent erosion model is significantly better than the nonlinear erosion model, but  $\gamma_K$  values are more than twice as high as the ones of the linear erosion model under the observed conditions. For all models with erosion formulations based on Eq. 5, the identifiability improves when the settling parameters  $w_{s,\text{fast}}$ ,  $w_{s,\text{slow}}$ , and  $\alpha$  are not part of the parameters to be identified (Table 5). We, therefore, recommend the use of the flux amplification

method to determine the properties of the sediment suspended in the water column first and then determine the parameters of the erosion models in a second step.

In our in situ study, we found that the use of all erosion models resulted in similarly good predictions of the observed data. As the identifiability of the nonlinear erosion model parameters is very low, we consider it as the least suitable model to describe sediment transport at our field site. In terms of identifiability, the linear erosion model with constant depth-independent coefficients performed best. The depth-dependent erosion model was less well identifiable. In addition, the parameters of the linear erosion model were in the middle of the range of the depth-dependent  $\tau_{\text{crit}}$  and  $M$  values of the depth-dependent erosion model. Fitting the parameters of the depth-dependent erosion model in fall also predicts almost constant values of  $\tau_{\text{crit}}$  and  $M$  throughout the sediment bed which was eroded during the observation period. If  $M$  was assumed to be constant with depth, the parameter fitting provided  $\beta$  values below  $5 \times 10^{-10} \text{ Pa g}^{-1} \text{ m}^2$  which resulted in changes of  $\tau_{\text{crit}}$  below  $1.5 \times 10^{-7} \text{ Pa}$ . These findings clearly indicate that the linear erosion model is the most suitable erosion model to describe sediment transport under the conditions observed during our field campaigns.

### Sediment bed properties

The identified parameters for the linear bed erosion model were similar to those observed by other studies of cohesive sediments. Zimmerman et al. (2008) measured a critical shear stress  $\tau_{\text{crit}}$  of  $1 \times 10^{-1} \text{ Pa}$  at a similar field site in South San Francisco Bay using an erosion chamber. This value compared well with  $\tau_{\text{crit}}$  observed in our study ( $1.1 \times 10^{-1} \text{ Pa}$  in spring and  $6.77 \times 10^{-2} \text{ Pa}$  in fall). In a study in Chesapeake Bay, Sanford and Halka (1993) measured critical shear stress values ranging from  $2.5 \times 10^{-2} \text{ Pa}$  to  $1.1 \times 10^{-1} \text{ Pa}$ .

**Table 5.** Collinearity indices  $\gamma_K$  for the different models and parameter combinations. All parameters: Settling velocities as well as the fine sediment fraction is considered in addition to the parameters of the erosion model.

	Flux amplification		Linear erosion model		Nonlinear erosion model		Depth-dependent erosion model	
Erosion parameters	—		$M, \tau_{crit}$		$M, k$		$M_{0r}, \mu, \tau_{crit,0r}, \beta$	
	Spring	Fall	Spring	Fall	Spring	Fall	Spring	Fall
All parameters	10.1	6.7	8.3	8.4	56	47	10.4	9.9
Erosion parameters	—	—	2.1	3.0	50	36	8.0	6.7

They observed erosion coefficients  $M$  for the linear erosion model (Eq. 7) of approximately  $0.300 \text{ g m}^{-2} \text{ s}^{-1} \text{ Pa}$ , which was also similar to our observations ( $0.274 \text{ g m}^{-2} \text{ s}^{-1} \text{ Pa}$  and  $0.99 \text{ g m}^{-2} \text{ s}^{-1} \text{ Pa}$  in spring and fall, respectively). The exponent  $k$  of the nonlinear erosion formulation (2.03 in spring and 1.33 in fall, Eq. 8) was also comparable to those observed by Sanford and Halka (1993) (between 1.3 and 4). As the erosion coefficient  $M$  of the nonlinear model depended strongly on the exponent, a direct comparison of these values is not applicable for different values of  $k$ . Both the linear and nonlinear models reproduced the general trends of sediment fluxes and sediment concentrations equally well (Fig. 9). The good performance of the linear bed erosion model (Fig. 10) might have been mainly due to the relatively small thickness of the eroded sediment bed. Assuming a porosity of 0.95, a solid mass density of  $2400 \text{ kg m}^{-3}$ , and a water density of  $1020 \text{ kg m}^{-3}$ , we obtained a maximum erosion depth of 0.006 m for the observed peak concentrations of  $150 \text{ g m}^{-3}$ . About 40% of this layer was regularly resuspended during periods of high tidal energy even in the absence of wind. This regular resuspension likely produced a low, almost constant critical shear stress in the topmost sediment layer.

Our data analysis highlighted the variability of sediment bed properties between the two campaigns. The bed roughness was lower during spring than fall, while the response of sediment erosion to bed shear stress was generally lower during fall. The exact reasons for these changes are still unclear. Brennan et al. (2002) showed in a study in northern San Francisco Bay that sediment erodibility may vary even over the diurnal tidal cycle. They suggested that this change may be due to the difference in salinity between 8 PSU during ebb and 14 PSU during flood. Still, at our field site salinities were around 28 PSU in spring and 31 PSU in Fall. We consider these differences to be too small to explain a difference in erodibility. A frequent explanation for the variation of erodibility in San Francisco Bay is the input of sediment from tributaries during large freshwater flows in winter (Schoellhamer 2002). This freshly deposited sediment is weakly consolidated and thus more easily erodible. In fact, there was some sediment influx to the system before the deployment in spring (Schoellhamer pers. comm.) which may explain the greater erodibility.

The increase in surface roughness and the decrease in sediment erodibility is consistent with a decrease of fine sediment content in the bed due to winnowing in spring and summer, as has been observed during the summer months at comparable field sites in the San Francisco South Bay by Nichols and Thompson (1985). However, the distribution of disaggregated grain size in the sediment bed was almost identical during both campaigns (data not shown) suggesting that the increase in roughness was instead due to perturbations of the muddy bed, perhaps of biologic origin.

### Significance to Aquatic Environments

The dynamics of sediment resuspension and settling plays an important role in estuarine systems. These processes govern nutrient supply (Wainright and Hopkinson 1997) and light availability (Cloern 1987) as well as the release of contaminants (Schoellhamer et al. 2007). In addition, the interplay between tides, windwave induced resuspension and particle settling will determine whether an estuary will accrete or loose sediments (Lacy et al. 1996), which is mainly important for the restoration and future fate of wetlands and intertidal marshes (Ganju et al. 2005).

In this manuscript, we present an approach to investigate sediment resuspension and settling dynamics based on concentrations and turbulent fluxes measured by ADVs using a simple, 1D mixing model. In situ particle size measurements using a LISST as well as the good performance of the two particle class model suggest that particles with different sizes are eroded from the bed and that no coagulation of particles occurred in the water column.

The basic assumption of the flux amplification method is the simultaneous occurrence of erosion and deposition as it is commonly used to describe sediment bed dynamics in natural environments (Winterwerp and van Kesteren 2004; Amoudry and Souza 2011). In addition, it is necessary that the measured fluxes reflect the processes occurring at the local sediment surface. This means that vertical sediment gradients should not be disturbed by horizontal advection as it might be the case in horizontally heterogeneous systems.

In addition to the sediment-bed erosion itself, the flux amplification factor  $\text{amp}$  (Eq. 9) depends on the settling velocity of the particles as well as on the sensor height.



Parameter fitting of the measured data based on the ADV mounted in 0.72 m of elevation resulted in an increase of the flux amplification factor by 0.1–0.2. This is due to the decrease of the sediment concentration gradient with increasing elevation above the sediment. Therefore, the factor amp itself is not suitable for a comparison of sediment properties recorded under different conditions, but the flux amplification method (Eq. 9) allows us to extrapolate sediment erosion rates from turbulent sediment fluxes observed above the sediment bed. Therefore, the method is useful for the detection of changes in the erodibility (the response of the bed erosion flux to the bed shear stress) such as occurred between spring and fall and the parameterization of linear and nonlinear bed erosion models (Eqs. 7 and 8).

As in many in situ observations, our approach could only reflect the dynamics under the conditions of the observation periods. To improve the predictive quality of the models, additional resuspension experiments using erosion carousels and flumes should be conducted which can cover a larger range of bottom stresses and allow a controlled temporal variation of bed stress dynamics. For example, a stepwise increase of bed shear stress allows distinguishing between Type I and Type II erosion (Parchure and Mehta 1985), which is difficult for our in situ observations in tidal systems, as the bottom shear stress varies continuously. A combination of carefully interpreted in situ observations as presented in this manuscript with sediment erosion experiments is desirable for a comprehensive characterization of sediment and particle dynamics. Controlled experiments allow a thorough characterization of the sediment erosion under a wide range of conditions, while disturbance free in situ investigations can be used as a check of the transferability of the erosion experiments to undisturbed field conditions.

### Appendix: Calculation and Adaption of the Grid Cell Size

The overall change in tidal elevation  $\Delta H$  over a time interval  $\Delta t$  is reflected by the horizontal gradient of the horizontal flow velocity in each cell

$$\Delta H = \int \int_{\Delta t H} \frac{\partial u(z)}{\partial x} dz dt \quad (\text{A.1})$$

Analogously, the change of height  $h$  of each individual cell is

$$\Delta h = \int \int_{\Delta t h} \frac{\partial u(z)}{\partial x} dz dt \quad (\text{A.2})$$

Assuming that the horizontal velocity gradient is proportional to the horizontal velocity

$$\frac{\partial u(z)}{\partial x} = Ku(z), \quad (\text{A.3})$$

we can calculate  $K$  by combining Eq. A.1 and A.3

$$K = \Delta H / \int \int_{\Delta t H} u(z) dz dt. \quad (\text{A.4})$$

Discretizing and combining Eqs. A.2, A.3, and A.4 leads to a change in size of the  $j$ th grid cell over a time step  $n$

$$\Delta h_j^{n+1} = \frac{\Delta H}{\sum_i u(z_i) h_i^n} u(z_j) h_j^n, \quad (\text{A.5})$$

where  $z_i$  and  $z_j$  are the elevations of the center of the grid cell. Therefore, the new thickness of the  $j$ th cell is:

$$h_j^{n+1} = h_j^n + \Delta h_j^{n+1} = h_j^n + \frac{\Delta H}{\sum_i u(z_i) h_i^n} u(z_j) h_j^n \quad (\text{A.6})$$

As we assume no horizontal concentration gradients, the sediment concentration is set to its old value  $C_j^{n+1/2} = C_j^n$  after adjusting the grid cell size (denoted by  $n+1/2$ ). The vertical velocity profiles were calculated using

$$u(z) = \frac{u_*}{\kappa} \ln \left( \frac{z}{z_R} \right) + u(z_R). \quad (\text{A.7})$$

where  $z_R$  is the height of the velocity  $u(z_R)$ . In our study  $z_R$  is 0.36 m. In the presented article, we used 60 grid cells. The initial size of the grid cells was calculated using

$$h_j^0 = \frac{H}{\sum_i u(z_i)} u(z_j), \quad (\text{A.8})$$

resulting in a nonequidistant initial grid spacing.

### References

- Agrawal, Y. C., and H. C. Pottsmith. 2000. Instruments for particle size and settling velocity observations in sediment transport. *Mar. Geol.* **168**: 89–114. doi:[10.1016/S0025-3227\(00\)00044-X](https://doi.org/10.1016/S0025-3227(00)00044-X)
- Amoudry, L. O., and A. J. Souza. 2011. Deterministic coastal morphological and sediment transport modeling: A review and discussion. *Rev. Geophys.* **49**: RG 2002. doi:[10.1029/2010RG000341](https://doi.org/10.1029/2010RG000341)
- Brand, A., J. R. Lacy, K. Hsu, D. Hoover, S. Gladding, and M. Stacey. 2010. Wind-enhanced resuspension in the shallow waters of South San Francisco Bay: Mechanisms and potential implications for cohesive sediment transport. *J. Geophys. Res.* **115**: C11024. doi:[10.1029/2010JC006172](https://doi.org/10.1029/2010JC006172)
- Brennan, M. L., D. H. Schoellhamer, J. R. Bureau, and S. G. Monismith. 2002. Tidal asymmetry and variability of bed shear stress and sediment bed flux at a site in San Francisco Bay, USA. In J. C. Winterwerp and C. Kranenburg [eds.], *Fine Sediment dynamics in the marine environment*. Elsevier Science.

- Bricker, J. D., S. Inagaki, and S. G. Monismith. 2005. Bed drag coefficient variability under wind waves in a tidal estuary. *J. Hydraulic Eng. ASCE* **131**: 497–508. doi:[10.1061/\(ASCE\)0733-9429\(2005\)131:6\(497\)](https://doi.org/10.1061/(ASCE)0733-9429(2005)131:6(497))
- Brun, R., P. Reichert, and H. R. Künsch. 2001. Practical identifiability analysis of large environmental simulation models. *Water Resour. Res.* **37**: 1015–1030. doi:[10.1029/2000WR900350](https://doi.org/10.1029/2000WR900350)
- Cartwright, G. M., C. T. Friedrichs, and S. J. Smith. 2013. A test of the ADV-based Reynolds-flux method for in situ estimation of sediment settling velocity in a muddy estuary. *Geo-Mar. Lett.* **33**: 477–484. doi:[10.1007/s00367-013-0340-4](https://doi.org/10.1007/s00367-013-0340-4)
- Cheng, R. T., C. H. Ling, J. W. Gartner, and P. F. Wang. 1999. Estimates of bottom roughness length and bottom shear stress in South San Francisco Bay, California. *J. Geophys. Res. Oceans* **104**: 7715–7728. doi:[10.1029/1998JC900126](https://doi.org/10.1029/1998JC900126)
- Cloern, J. E. 1987. Turbidity as a control on phytoplankton biomass and productivity in estuaries. *Cont. Shelf Res.* **7**: 1367–1381. doi:[10.1016/0278-4343\(87\)90042-2](https://doi.org/10.1016/0278-4343(87)90042-2)
- Drake, D. E., and D. A. Cacchione. 1989. Estimates of the suspended sediment reference concentration ( $C_a$ ) and resuspension coefficient ( $g_0$ ) from near-bottom observations on the California shelf. *Cont. Shelf Res.* **9**: 51–64. doi:[10.1016/0278-4343\(89\)90082-4](https://doi.org/10.1016/0278-4343(89)90082-4)
- Dyer, K. R., and R. L. Soulsby. 1988. Sand transport on the continental shelf. *Annu. Rev. Fluid Mech.* **20**: 295–324. doi:[10.1146/annurev.fl.20.010188.001455](https://doi.org/10.1146/annurev.fl.20.010188.001455)
- Fugate, D. C., and C. T. Friedrichs. 2002. Determining concentration and fall velocity of estuarine particle populations using ADV, OBS and LISST. *Continental Shelf Research* **22**: 1867–1886. doi:[10.1016/S0278-4343\(02\)00043-2](https://doi.org/10.1016/S0278-4343(02)00043-2)
- Ganju, N. K., D. R. Schoellhamer, and B. Bergamaschi. 2005. Suspended sediment fluxes in a tidal wetland: Measurement, controlling factors, and error analysis. *Estuaries Coast* **28**: 812–822. doi:[10.1007/BF02696011](https://doi.org/10.1007/BF02696011)
- Ha, H. K. and J. P.-Y. Maa. 2009. Evaluation of two conflicting paradigms for cohesive sediment deposition. *Mar. Geol.* **265**: 120–129. doi:[10.1016/j.margeo.2009.07.001](https://doi.org/10.1016/j.margeo.2009.07.001)
- Ha, H. K. and J. P.-Y. Maa. 2010. Effects of suspended sediment concentration and turbulence on settling velocity of cohesive sediment. *Geosci. J.* **14**: 163–171. doi:[10.1007/s12303-010-0016-2](https://doi.org/10.1007/s12303-010-0016-2)
- Kineke, G. C., and R. W. Sternberg. 1989. The effect of particle settling velocity on computed suspended sediment concentration profiles. *Mar. Geol.* **90**: 159–174. doi:[10.1016/0025-3227\(89\)90039-X](https://doi.org/10.1016/0025-3227(89)90039-X)
- Kleeberg, A., M. Hupfer, and G. Gust. 2008. Quantification of phosphorus entrainment in a lowland river by in situ and laboratory resuspension experiments. *Aquat. Sci.* **70**: 87–99. doi:[10.1007/s00027-007-0935-9](https://doi.org/10.1007/s00027-007-0935-9)
- Kranck, K., and T. G. Milligan. 1992. Characteristics of suspended particles at an 11-hour anchor station in San Francisco Bay, California. *J. Geophys. Res.* **97**: 11,373–11,382. doi:[10.1029/92JC00950](https://doi.org/10.1029/92JC00950)
- Lacy, J. R., S. Gladding, A. Brand, A. Collignon, and M. Stacey. 2014. Lateral baroclinic forcing enhances sediment transport from shallows to channel in an estuary, *Estuaries Coast* **37**: 1058–1077. doi:[10.1007/s12237-013-9748-3](https://doi.org/10.1007/s12237-013-9748-3)
- Lacy, J. R., D. R. Schoellhamer, and J. R. Burau. 1996. Suspended-solids flux at a shallow-water side in South San Francisco Bay, California, Proceedings of the North American Water and Environment Congress '96. American Society of Civil Engineers, New York.
- Lee, X., W. Massmann, and B. Law. 2004. Handbook of micrometeorology—a guide for surface flux measurement and analysis. Kluwer.
- MacVean, L. J., and J. R. Lacy. 2014. Interactions between waves, sediment, and turbulence on a shallow estuarine mudflat. *J. Geophys. Res. Oceans* **119**: 1534–1553. doi:[10.1002/2013JC009477](https://doi.org/10.1002/2013JC009477)
- Manning, A. J., and K. R. Dyer. 2007. Mass settling flux of fine sediments in Northern European estuaries: Measurements and predictions. *Mar. Geol.* **245**: 107–122. doi:[10.1016/j.margeo.2007.07.005](https://doi.org/10.1016/j.margeo.2007.07.005)
- Manning, A. J., D. H. Schoellhamer, A. J. Mehta, D. Nover, and S. G. Schladow. 2010. Video measurements of flocculated sediment in lakes and estuaries in the USA. Proceedings of the 4th Federal Interagency Hydrologic Modeling Conference and the 9th Federal Interagency Sedimentation Conference Las Vegas, NV, June 27–July 1, 2010. Available from [http://acwi.gov/sos/pubs/2ndJFIC/Contents/10A\\_Manning\\_05April2010\\_MANUSCRIPT\\_update\\_10\\_paper.pdf](http://acwi.gov/sos/pubs/2ndJFIC/Contents/10A_Manning_05April2010_MANUSCRIPT_update_10_paper.pdf). Last accessed on March 13, 2014.
- Murphy, A. H., and E. S. Epstein. 1989. Skill scores and correlation coefficients in model verification. *Monthly Weather Rev.* **117**: 572–582. doi:[10.1175/1520-0493\(1989\)1172.0.CO;2](https://doi.org/10.1175/1520-0493(1989)1172.0.CO;2)
- Nichols, F. H., and J. K. Thompson. 1985. Time scales of change in the San Francisco Bay benthos. *Hydrobiologia* **129**: 121–138. doi:[10.1007/BF00048691](https://doi.org/10.1007/BF00048691)
- Ogilvie, B. G., and S. F. Mitchell. 1998. Does sediment resuspension have persistent effects on phytoplankton? Experimental studies in three shallow lakes. *Freshw. Biol.* **40**: 51–63. doi:[10.1046/j.1365-2427.1998.00331.x](https://doi.org/10.1046/j.1365-2427.1998.00331.x)
- Parchure, T. M. and A. J. Mehta. 1985. Erosion of soft cohesive sediment deposits. *J. Hydraulic Eng.* **111**: 1308–1326. doi:[10.1061/\(ASCE\)0733-9429\(1985\)111:10\(1308\)](https://doi.org/10.1061/(ASCE)0733-9429(1985)111:10(1308))
- Pejrup, M., and O. A. Mikkelsen. 2010. Factors controlling the field settling velocity of cohesive sediment in estuaries. *Estuar. Coast. Shelf Sci.* **87**: 177–185. doi:[10.1016/j.ecss.2009.09.028](https://doi.org/10.1016/j.ecss.2009.09.028)
- Sanford, L. P., and J. P. Halka. 1993. Assessing the paradigm of mutually exclusive erosion and deposition of mud, with examples from upper Chesapeake Bay. *Mar. Geol.* **114**: 37–57. doi:[10.1016/0025-3227\(93\)90038-W](https://doi.org/10.1016/0025-3227(93)90038-W)

- Sanford, L. P., and J. P.-Y. Maa. 2001. A unified erosion formulation for fine sediments. *Mar. Geol.* **179**: 9–23. doi:[10.1016/S0025-3227\(01\)00201-8](https://doi.org/10.1016/S0025-3227(01)00201-8)
- Sanford, L. P. 2008. Modeling a dynamically varying mixed sediment bed with erosion, deposition, bioturbation, consolidation, and armoring. *Comput. Geosci.* **34**: 1263–1283. doi:[10.1016/j.cageo.2008.02.011](https://doi.org/10.1016/j.cageo.2008.02.011)
- Schoellhamer, D. H. 2002. Variability of suspended-sediment concentration at tidal to annual time scales in San Francisco Bay, USA. *Cont. Shelf Res.* **22**: 1857–1866. doi:[10.1016/S0278-4343\(02\)00042-0](https://doi.org/10.1016/S0278-4343(02)00042-0)
- Schoellhamer, D. H., T. E. Mumley, and J. E. Leatherbarrow. 2007. Suspended sediment and sediment-associated contaminants in San Francisco Bay. *Environ. Res.* **105**: 119–131. doi:[10.1016/j.envres.2007.02.002](https://doi.org/10.1016/j.envres.2007.02.002)
- Shaw, W. J., and J. H. Trowbridge. 2001. The direct estimation of near-bottom turbulent fluxes in the Presence of Energetic Wave Motions. *J. Atmos. Oceanic Technol.* **18**: 1540–1557. doi:[10.1175/1520-0426\(2001\)018<1540:TDEONB>2.0.CO;2](https://doi.org/10.1175/1520-0426(2001)018<1540:TDEONB>2.0.CO;2)
- Sherwood, C. R., J. R. Lacy, and G. Voulgaris. 2006. Shear velocity estimates on the inner shelf of Grays Harbor, Washington, USA. *Cont. Shelf Res.* **26**: 1995–2018. doi:[10.1016/j.csr.2006.07.025](https://doi.org/10.1016/j.csr.2006.07.025)
- Sternberg, R. W., D. A. Cacchione, D. E. Drake, and K. Kranck. 1986. Suspended sediment transport in an estuarine tidal channel within San Francisco Bay, California. *Mar. Geol.* **71**: 237–258. doi:[10.1016/0025-3227\(86\)90072-1](https://doi.org/10.1016/0025-3227(86)90072-1)
- Styles, R., and S. M. Glenn. 2000. Modeling stratified wave and current bottom boundary layers on the continental shelf. *J. Geophys. Res. Oceans* **110**: 24119–24139. doi:[10.1029/2000JC900115](https://doi.org/10.1029/2000JC900115)
- Tengberg, A., E. Almroth, and P. Hall. 2003. Resuspension and its effects on organic carbon recycling and nutrient exchange in coastal sediments: in situ measurements using new experimental technology. *J. Exp. Mar. Biol. Ecol.* **285–286**: 119–142. doi:[10.1016/S0022-0981\(02\)00523-3](https://doi.org/10.1016/S0022-0981(02)00523-3)
- Tolhurst, T. J., K. S. Black, and D. M. Paterson. 2009. Muddy sediment erosion: Insights from field studies. *J. Hydraulic Eng.* **135**: 73–87. doi:[10.1061/\(ASCE\)0733-9429\(2009\)135:2\(73\)](https://doi.org/10.1061/(ASCE)0733-9429(2009)135:2(73))
- Van Prooijen, B. C., and J. C. Winterwerp. 2010. A stochastic formulation for erosion of cohesive sediments. *J. Geophys. Res.* **115**: C01005. doi:[10.1029/2008JC005189](https://doi.org/10.1029/2008JC005189)
- Wainright, S. C., and C. S. Hopkinson. 1997. Effects of sediment resuspension on organic matter processing in coastal environments: A simulation model. *J. Mar. Syst.* **11**: 353–368. doi:[10.1016/S0924-7963\(96\)00130-3](https://doi.org/10.1016/S0924-7963(96)00130-3)
- Wiberg, P. L., D. E. Drake, and D. A. Caccione. 1994. Sediment resuspension and bed armouring during high bottom stress events on the northern California inner continental shelf-Measurements and predictions. *Cont. Shelf Res.* **14**: 1191–1219. doi:[10.1016/0278-4343\(94\)90034-5](https://doi.org/10.1016/0278-4343(94)90034-5)
- Wiberg, P. L., and C. R. Sherwood. 2008. Calculating wave-generated bottom orbital velocities from surface-wave parameters. *Comput. Geosci.* **34**: 1243–1262. doi:[10.1016/j.cageo.2008.02.010](https://doi.org/10.1016/j.cageo.2008.02.010)
- Wiberg, P. L., and J. D. Smith. 1983. A comparison of field data and theoretical models for wave-current interactions at the bed on the continental shelf. *Cont. Shelf Res.* **2**: 147–162. doi:[10.1016/0278-4343\(83\)90013-4](https://doi.org/10.1016/0278-4343(83)90013-4)
- Winterwerp, J. C., and van Kesteren. 2004. Introduction to the physics of cohesive sediment in the marine environment. *Developments in Sedimentology Series*, v. **56**. Elsevier.
- Zimmerman, J. R., J. D. Bricker, C. Jones, P. J. Dacunto, R. L. Street, and R. G. Luthy. 2008. The stability of marine sediments at a tidal basin in San Francisco Bay amended with activated carbon for sequestration of organic contaminants. *Water Res.* **42**: 4133–4145. doi:[10.1016/j.watres.2008.05.023](https://doi.org/10.1016/j.watres.2008.05.023)

### Acknowledgments

This study was financed by the Swiss National Science Foundation (grant Nr. PBEZ2-121244) and the Deutsche Forschungsgemeinschaft (grant Nr. BR3785/1-1). The field work and part of the associated analysis was funded by NSF (OCE-0751970). We thank Audric Collignon, Dan Hoover, Lissa MacVean, Joanne Ferreira, Tim Elfers and Jim Christmann for support in the field. We thank David Schoellhamer, Lissa McVean and one anonymous reviewer and Carl Friedrichs for their helpful comments.

Submitted 17 March 2014

Revised 9 September 2014

Accepted 30 October 2014

Associate editor: Stephen Monismith